Hall C Proposal to PAC37

The Neutron Electric Form Factor at Q^2 up to 7 $(\mathrm{GeV/c})^2$ from the Reaction $^2H(\vec{e}, e'\vec{n})^1H$ via Recoil Polarimetry

Spokepersons:

B. D. Anderson (Kent State University), J. Arrington (Argonne National Lab.), S. Kowalski (MIT), R. Madey (Kent State University), B. Plaster (University of Kentucky), A.Yu. Semenov (University of Regina)

Abstract

We propose to extend our previous measurements of G_E^n from deuterium to $Q^2 = 6.88$ $(\mathrm{GeV/c})^2$. Additional measurements at 5.22 and 3.95 $(\mathrm{GeV/c})^2$ will provide continuity with our prior measurements up to $Q^2 = 1.45$ $(\mathrm{GeV/c})^2$, and overlap with recent measurements from a polarized ^3He target.

The JLab E93-038 collaboration measured G_E^n from the $d(\vec{e}, e'\vec{n})p$ reaction on a liquid deuterium target at Q^2 values of 0.45, 1.13, and 1.45 $(\mathrm{GeV/c})^2$. The experiment used a high-luminosity neutron polarimeter and the dipole neutron-spin-precession magnet [Charybdis] to measure the ratio of two scattering asymmetries associated with positive and negative precessions of the neutron polarization vector. In this ratio technique, systematic uncertainties are extremely small because the analyzing power of the polarimeter cancels in the ratio, and sensitivity to the beam polarization is reduced because it depends only on the small drift in polarization between sequential measurements. Use of a deuteron target yields a better separation between quasielastic and inelastic events, as well as a smaller proton background which must be cleanly separated from the neutron scattering events. Finally, the reaction mechanism and nuclear physics corrections [for FSI, MEC, and IC] are best understood and can be most reliably corrected for in the deuteron. The combination of these advantages is what yields 2–3% systematic uncertainties for the recoil polarization measurement, while the polarized ^{3}He measurements typically have $\approx$10% systematic uncertainties.

The primary motivation for this proposed experiment is the ability to measure a fundamental quantity of the neutron – one of the basic building blocks of matter. A successful model of confinement must be able to predict both neutron and proton electromagnetic form factors simultaneously. The neutron electric form factor is especially sensitive to the nucleon wave function, and differences between model predictions for G_E^n tend to increase rapidly with Q^2. Calculations and fits to the data up to 1.45 $(\mathrm{GeV/c})^2$ show significant quantitative differences in the few $(\mathrm{GeV/c})^2$ range, and make qualitatively different predictions for the behavior of G_E^n at higher Q^2 values, with some showing G_E^n falling off more slowly than G_M^n, and others showing G_E^n falling rapidly to zero and becoming negative. The proposed measurements of G_E^n will be able to challenge theoretical calculations, including both models and new rigorous lattice QCD calculations, with a focus on the high Q^2 range where the models of the nucleon are generally meant to be more complete. Finally, these measurements of G_E^n are also needed to understand electron scattering experiments that probe electric structure functions at high Q^2, and will be important for the analysis of precision few-body data from measurements at Jefferson Lab.

List of Participants

R. Madey (Spokesman), B.D. Anderson (Co-Spokesman and Institutional Representative), A.R. Baldwin, D.M. Manley, J.W. Watson, W.-M. Zhang, Graduate Student

Kent State University

R. Carlini (Institutional Representative), S. Covrig, R. Ent, H. Fenker, D. Gaskell, M. Jones, D. Higinbotham, A. Lung, D. Mack, J. Mei, G. Smith, P. Solvignon, S. Taylor, S. Wood

Thomas Jefferson National Accelerator Facility

S. Kowalski (Co-Spokesman and Institutional Representative), Graduate Student

Massachusetts Institute of Technology

B. Plaster (Co-Spokesman and Institutional Representative), W. Korsch, Graduate Student

University of Kentucky

A.Yu. Semenov (Co-Spokesman and Institutional Representative), G. Huber, G.J. Lolos, Z. Papandreou, I.A. Semenova, Graduate Student

University of Regina

C. Howell (Institutional Representative), Postdoc

Duke University

J. Arrington (Co-Spokesman and Institutional Representative), K. Hafidi, R. Holt, P. Reimer

Argonne National Laboratory

C. Perdrisat (Institutional Representative), W. Deconinck

The College of William and Mary

C. Keppel (Institutional Representative), L. Tang, I. Albayrak, O. Ates, C. Chen, M.E. Christy, M. Kohl, Y. Li, A. Liyanage, Z. Ye, T. Walton, L. Yuan, L. Zhu

Hampton University

A. Ahmidouch (Institutional Representative), S. Danagoulian, A. Gasparian

North Carolina A&T State University

List of Participants (continued)

M. Elaasar

Southern University at New Orleans

H. Arenhovel

University of Mainz

H.G. Mkrtchyan (Institutional Representative), V. Tadevosyan, A. Asaturyan, A. Mkrtchyan, S. Zhamkochyan

Yerevan Physics Institute

S. Wells (Institutional Representative), N. Simicevic

Louisiana Tech

P. Markowitz (Institutional Representative), B. Raue, J. Reinhold

Florida International University

D. Day (Institutional Representative), O. Rondon

University of Virginia

W. Tireman

Northern Michigan University

S. Tajima

Los Alamos National Laboratory

M. Khandaker (Institutional Representative), V. Punjabi

Norfolk State University

R.E. Segel

Northwestern University

R. Wilson

Harvard University

L. Gan

University of North Carolina at Wilmington

List of Participants (continued)

A.I. Malakhov (Institutional Representative), A.K. Kurilkin, P.K. Kurilkin, V.P. Ladygin, S.M. Piyadin.

Joint Institute for Nuclear Research (Dubna)

J. Martin

University of Winnipeg

S. Jin, W.-Y. Kim (Institutional Representative), S. Stepanyan, S. Yang, Graduate Student

Kyungpook National University

H. Breuer

University of Maryland

T. Reichelt

University of Bonn

I. Sick

University of Basel

F.R. Wesselmann

Xavier University of Louisiana

K. McCormick

Pacific Northwest National Laboratory

CONTENTS

List of Figures

List of Tables

1 Introduction

PAC 26 approved E04-110 to measure the electric form factor of the neutron, G_E^n, at a squared four-momentum transfer, Q^2, of 4.3 (GeV/c)^2 via recoil polarimetry with a liquid deuterium target. The jeopardy resubmission to PAC 33 was deferred with regret because it could not be fit into the schedule with the 6 GeV beam. PAC 34 approved our original 11 GeV proposal, PR12-09-006, to measure G_E^n at Q^2 values up to 6.88 (GeV/c)^2, stating that our proposal "to measure G_E^n by recoil polarimetry in Hall C is again a benchmark measurement". PAC 35 declined to rate this proposal, and recommended that we submit a more detailed update on the polarimeter design. This new proposal addresses the concerns of PAC 35, and includes detailed simulation studies of the updated polarimeter design. Here, we now again propose to extend measurements of G_E^n to a Q^2 value of 6.88 (GeV/c)^2 with additional measurements at lower Q^2 values to provide continuity with the previous measurements on deuterium and to provide overlap with the E02-013 polarized ^3He data that has recently been reported at Q^2 values up to 3.41 (GeV/c)^2 [Riordan et al. (2010)]. Measurements at $Q^2 = 3.95$, 5.22, and 6.88 (GeV/c)^2 can be made in a time of 10, 15, and 30 days, respectively. The projected uncertainties in G_E^n are about 0.001, and smaller than those in the E02-013 measurement at their three (recently reported) Q^2 points of 1.72, 2.48, and 3.41 (GeV/c)^2. The systematic errors from the recoil polarimetry measurements with a liquid deuterium target are estimated to be small, and the total error would be completely statistics dominated.

The sytematic uncertainties in the recently reported E02-013 results are at the level of 9–11% [Riordan et al. (2010)]. Indeed, there is a ~ 2 standard deviation difference between the E93-038 result at $Q^2 = 1.45$ (GeV/c)^2 and the E02-013 result at $Q^2 = 1.72$ (GeV/c)^2. It is unlikely that this difference is due to the slightly different Q^2 values. Indeed, one can not say that one experiment (or the other, or both) is flawed; instead, the two techniques are sufficiently different, and there may be some not-yet-discovered systematic error. Thus, it is clear that further data, obtained with both our recoil polarization from deuterium technique, and the polarized ^{3}He technique, are warranted.

A significant merit of our technique is that the total systematic uncertainty in the neutron polarimeter measurements is typically 2.5% [as documented in detail in Appendix B]. At higher Q^2 values, high rates and larger backgrounds become more important issues. Much of the background is associated with scattering from the protons, which is minimized by making measurements on deuterium. For the proposed measurement, background and DAQ rates can be handled and clean identification of the quasielastic neutron events can be performed using well established techniques; we do not rely on any improvements over what has been demonstrated.

Our proposed measurements are in a most interesting region. Until the results of the polarized ^3He measurement are published, the world's data are limited to Q^2 values below 1.5 (GeV/c)^2. Extrapolations of the world's data suggest that G_E^n may exceed G_E^p somewhere in the range of 4–5 (GeV/c)^2 and consequently, the isovector electric form factor $[G_E^v \equiv G_E^p - G_E^n]$ would become negative. This idea is also supported by calculations, e.g. [Miller (2002)], which predict that the ratio G_E^n/G_M^n will continue to increase with increasing Q^2. Other calculations, e.g. [Lomon (2002)], suggest that the ratio G_E^n/G_M^n will level off somewhere above 2–3 (GeV/c)^2 or even decrease with G_E^n becoming negative somewhere above 4–5 (GeV/c)^2, as in the calculation of [Cloet et al. (2008)] or the duality-constrained fit of [Bodek et al. (2008)]. While calculations and fits show some differences in the 2–3 (GeV/c)^2 range, they predict *qualitatively different behavior* at even higher Q^2 values. Clearly, providing precise measurements of G_E^n in this range will strongly challenge the assumptions that go into these models. There is an added benefit to testing these models at high Q^2, as the low Q^2 behavior is believed to have

large contributions from pion cloud effects, and as such cannot directly evaluate models which do not include pion cloud effects or which make only estimates of these effects. At high Q^2, inconsistencies between the calculations and G_E^n measurements should directly test modeling of the the quark core, which is the focus of many of these calculations.

In summary, we are extending G_E^n measurements to $Q^2 = 6.9$ (GeV/c)^2 with extremaly small systematic uncertainties and a total uncertainty ($\Delta G_E^n = 0.001$). We will also obtain two other points at $Q^2 = 3.95$ and 5.22 (GeV/c)^2, which are close to measurements from the 6 GeV and 12 GeV polarized ^3He experiments. The measurements have small and well understood systematics, and requires the SHMS and an expanded recoil polarimeter, but do not rely on any R&D for new equipment or any special techniques to deal with rates or backgrounds.

2 Scientific Motivation and Background

2.1 Extension of E93-038 to Measure G_E^n up to $Q^2 = 7$ (GeV/c)^2

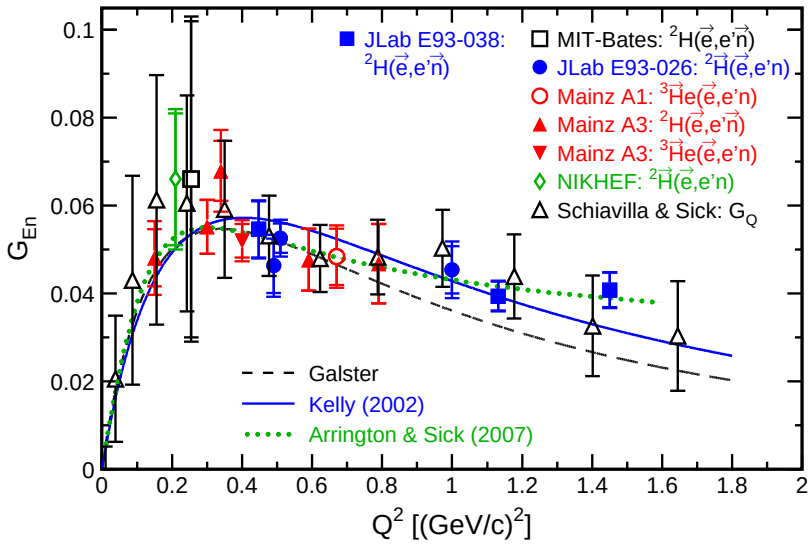

Figure 1: G_E^n versus Q^2. Data from E93-038 and world data. The black dashed line reflects the Galster parameterization; the blue solid line is our modified Galster fit (Kelly 2002); the green dotted line reflects the Arrington and Sick (2007) fit.

The electric form factor of the neutron, G_E^n, is a fundamental quantity needed for the understanding of both nucleon and nuclear structure. The dependence of G_E^n on Q^2 reflects the distribution of charge in the neutron. The E93-038 collaboration carried out measurements of G_E^n from September 8, 2000 to April 26, 2001 at three values of Q^2 [viz., 0.45, 1.13, and 1.45 (GeV/c)^2]. Results were reported in Physical Review Letters [Madey et al. (2003)], and in Physical Review C [Plaster et al. (2006)]. Data from E93-038 are plotted (as filled squares) in Fig. 1 together with the current world data extracted from polarization measurements [Eden et al. (1994), Herberg et al. (1999), Bermuth et al. (2003), Golak et al. (2001), Passchier et al. (1999), Zhu et al. (2001), Warren et al. (2004), Glazier et al. (2005)] and from an analysis of the deuteron quadrupole form factor [Schiavilla and Sick (2001)]. The projected uncertainties from PR12-09-016, the polarized ^3He target measurement in Hall A, are not shown in Fig. 1, as it is not clear what uncertainties or Q^2 values are appropriate. PAC35 approved the experiment

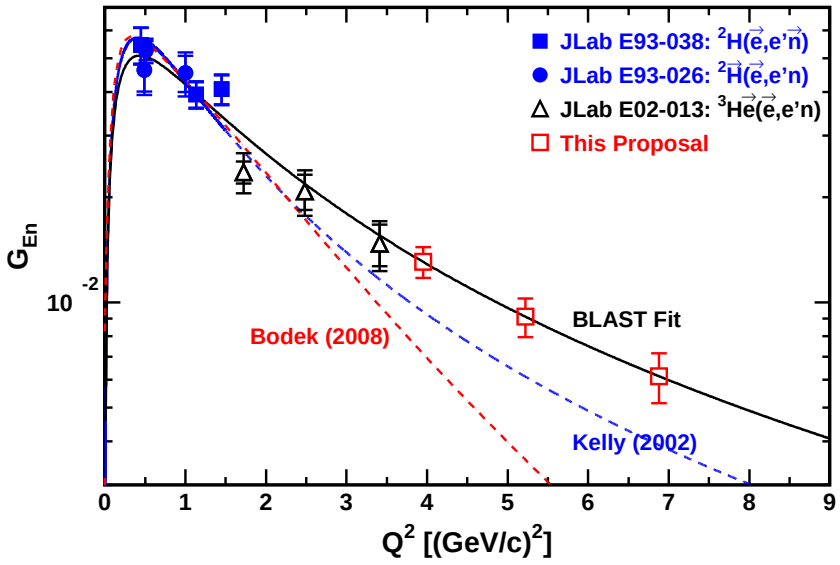

Figure 2: G_E^n versus Q^2. Data from JLab and projections from this proposal. The red line reflects the Bodek (2008) fit, the blue line is our modified Galster fit [Kelly (2002)], and solid black line reflects BLAST fit [Geis (2008)].

with reduced beamtime, with instructions to reduce the maximum Q^2 from 10.2 to ~8 GeV^2, and improve the uncertainties. However, for their lower Q^2 points, the statiatical (systematic) uncertainties were 18% (12.5%) at Q^2=5 GeV^2 and 13% (13.2%) at Q^2=6.8 GeV^2. Thus, even with increased running time at the lower Q^2 values, the uncertainties will be systematics limited; tripling the beam time would still yield ≥15% total uncertainties. Their projected systematic uncertainties were somewhat smaller (closer to 10%) in the update presented to PAC35, this is only a small improvement in the total acheiveable uncertainty.

We fitted the published results and the G_E^n slope at the origin as measured via low-energy neutron scattering from electrons in heavy atoms [Kopecky et al. (1997)] to a Galster et al. (1971) parameterization:

$$G_E^n = -a\mu_n\tau G_D/(1+b\tau), \tag{1}$$

where $\tau = Q^2/4M_n^2$, $G_D = (1+Q^2/\Lambda^2)^{-2}$, and $\Lambda^2 = 0.71$ (GeV/c)^2. Our best-fit parameters are a = 0.886±0.023 and b = 3.29±0.31 [Kelly (2003)]. More recent BLAST fit (shown in Fig. 2 as solid black line) utilizes whole available set of Gen data including the BLAST experiment results with improved precision at low Q^2 [Geis (2008)]. This parameterization is based on the sum of two dipoles, $\Sigma a_i/(1+Q^2/b_i)^2$, $(i=1,2)$. The parameter $a_1 = -a_2 = 0.095 \pm 0.018$ is constrained by the radius of neutron, $b_1 = 2.77 \pm 0.83$, and $b_2 = 0.339 \pm 0.046$. We use this parameterization for our estimations of expected asymmetries and uncertainties. Figure 3 shows the extracted values of the ratio $\mu_n G_E^n/G_M^n$, including the high Q^2 results from the E02-013 preprint [Riordan et al. (2010)].

The reported values of the ratio of the neutron electric to magnetic form factor ratio, G_E^n/G_M^n, represent both the highest Q^2 extraction and most precise published determinations of G_E^n. Even including the preliminary results from the polarized ^3He target measurements, the measurements from deuterium will represent the highest precision extractions, with relative statistical uncertainties of 8.4% and 9.5% at the two highest Q^2 points and extremely small systematic uncertainties of 2-3%. The small systematic uncertainties occur because a measurement from deuterium has a theoretical advantage and the use of a neutron polarimeter provides a significant experimental advantage. The use of a deuterium target yields smaller backgrounds (e.g.

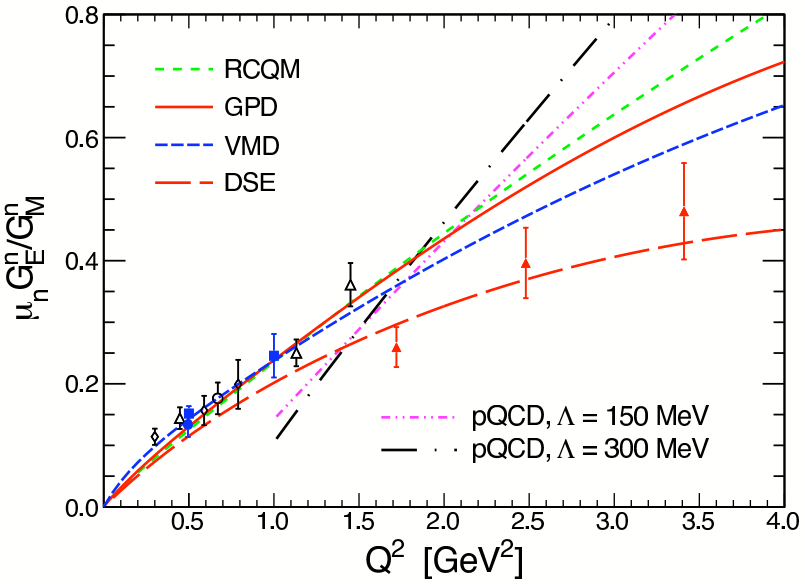

Figure 3: $\mu_n G_E^n/G_M^n$ versus Q^2, including the new e02013 results (figure from [Riordan et al. (2010)]).

from quasielastic scattering from a proton followed by a charge exchange reaction), as well as better separation between quasielastic and inelastic scattering. In addition, the quasielastic $^2\mathrm{H}(\vec{e}, e'\,\vec{n})^1\mathrm{H}$ reaction is insensitive to FSI, MEC, IC, and the choice of the NN potential for the deuteron wavefunction.

Experimentally, the polarimeter permits measurement of scattering asymmetries by the cross-ratio technique, which provides several advantages. In the cross-ratio technique, the asymmetry is calculated as the ratio of geometric means of the up and down scattering yields in the polarimeter for the two beam helicity states. The advantage of this technique is that the resulting value for the asymmetry is independent of the luminosities for the two electron beam helicity states and independent of the efficiencies and acceptances of the top and bottom halves of the polarimeter. Also contributing to the small systematic uncertainties in our technique is the fact that the analyzing power of the polarimeter and the polarization of the electron beam cancel in the asymmetries ratio, much like the recoil polarization measurements in elastic e–p scattering. Other sources of uncertainty, such as radiative corrections and neutron depolarization by the lead shielding, are small also because they nearly cancel in the ratio. (See Section 4 for more details.)

2.2 Better Understanding of Nucleon Structure

Different models of the nucleon correspond to different assumptions for the Dirac and Pauli form factors. Models with a two-term structure produce results in qualitative agreement with data; for example, a soliton model [Holzwarth (2002)], two relativistic constituent quark models [Miller (2002) and Cardarelli and Simula (2002)], and a model [Lomon (2002)] that couples vector meson dominance with the predictions of pQCD all have this structure and produce results in qualitative agreement with data. Predictions of these models are compared with data in Fig. 4. The chiral soliton model [Holzwarth (2002)] reproduces the dramatic linear decrease observed in $\mu_p G_E^p/G_M^p$ for $1 < Q^2 < 6$ (GeV/c)^2; however, this model fails to reproduce the neutron data at

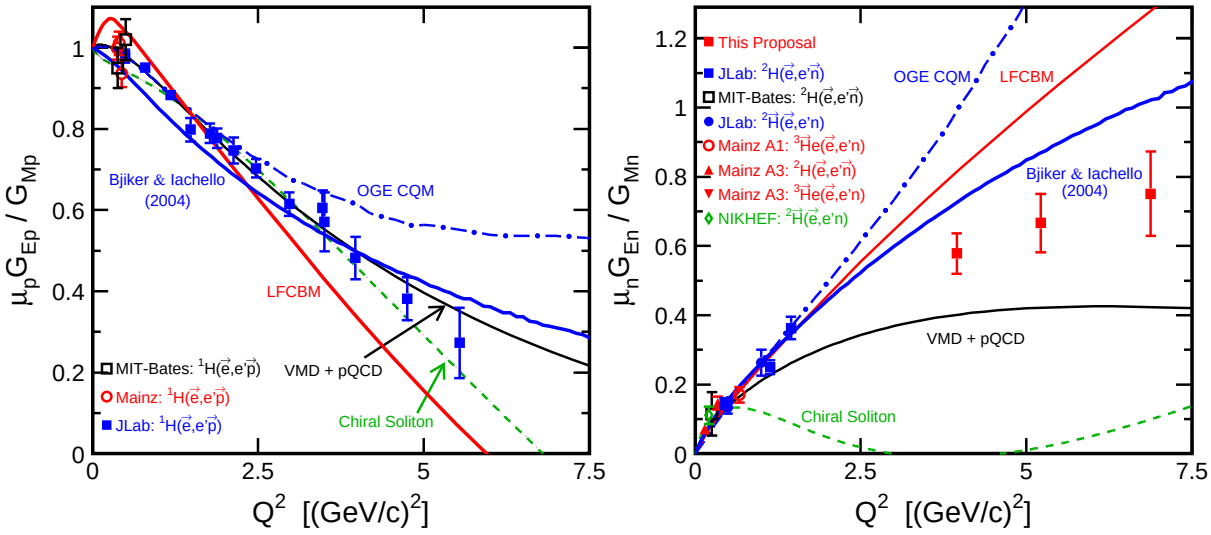

Figure 4: Predictions of selected models for $\mu_p G_E^p/G_M^p$ and $\mu_n G_E^n/G_M^n$ compared with proton and neutron data. Solid-red-box symbols in the right panel represent uncertainties of the proposed G_E^n measurements.

large Q^2. A light-front calculation using point-like constituent quarks surrounded by a cloud of pions [Miller (2002)], denoted "LFCBM", describes the neutron data, but falls below the proton data at high Q^2. A one-gluon exchange light-front calculation, denoted "OGE CQM", using constituent quark form factors fitted to $Q^2 < 1$ (GeV/c)^2 data [Cardarelli and Simula (2000)] agrees with the neutron data, but deviates from the proton data above $Q^2 \sim 3.0$ (GeV/c)^2. The Lomon model, denoted "VMD + pQCD", agrees with the proton data but falls below the neutron data above $Q^2 \sim 1.2$ (GeV/c)^2. Note that many of the available calculations do not include a pion cloud contribution, which are of particular importance for G_E^n. This means that quantitative comparisons with the data will be of limited use in the Q^2 range of the present data, and one wants to go beyond 3–4 (GeV/c)^2 to be able to directly confront these models with the complete set of proton and neutron form factor measurements.

Models of the nucleon structure make a wide range of predictions for G_E^n at high Q^2, from cases where $G_E^n/\mu_n G_M^n$ continues to grow almost linearly to well above 5 (GeV/c)^2, to those that show the ratio flattening or even turning over and changing sign. A very recent Fadeev calculation [Cloet et al. (2008)] predicts that the increase in G_E^n/G_M^n only extends to ∼4 (GeV/c)^2, and that the ratio begins to decrease around 5–6 (GeV/c)^2, with a predicted zero crossing near 11 (GeV/c)^2. Similarly, various parameterization of the form factors, e.g. the Galster form or the parameterization by Kelly, have $\mu_n G_E^n/G_M^n$ increasing with Q^2 but leveling off at high Q^2 values, while the recent BBBA08 parameterization [Bodek et al. (2008)] uses constraints for the high Q^2 limit and predicts, based on duality arguments, that $G_E^n/\mu_n G_M^n$ will level off near 3–4 (GeV/c)^2, and then will cross zero and change sign somewhere near 10 (GeV/c)^2.

Because the calculations and fits yield such a wide range of results, it is important to go to high Q^2 to evaluate these models. Preliminary results from the ^3He measurement (up to 3.4 (GeV/c)^2) are now available. The preliminary results suggested that between 1.5 and 3.5 (GeV/c)^2, G_E^n falls more rapidly than the Galster-like fits based on a modified dipole form. This was taken as an indication that G_E^n was beginning to fall more rapidly than G_M^n, similar to what has been observed in the falloff of the proton electric form factor. The current results from the analysis [Riordan (2010)] are significantly higher, and do not show such a falloff, although the uncertainties makes it difficult to reach a clear conclusion on this point. Even with final

results from the ^3He measurement, it will be critical to extend the measurements to higher Q^2 values where the models and parameterizations begin to show qualitatively different predictions. At 3.4 (GeV/c)^2, the difference between the Kelly parameterization and the BBBA08 is only 10–20%, while at 7 (GeV/c)^2, they differ by nearly a factor of two.

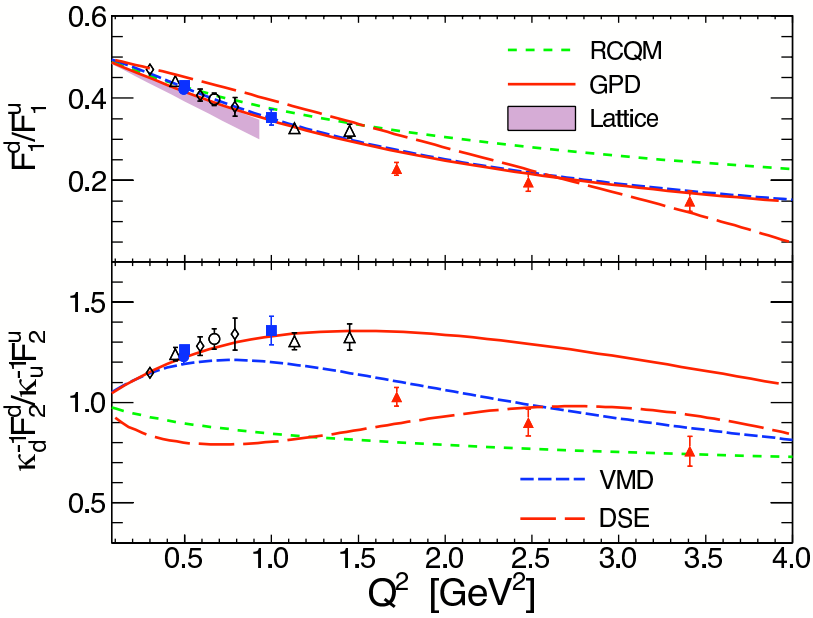

Figure 5: Ratio of the down quark to up quark contributions to F_1 and F_2 extracted from combined proton and neutron form factor measurements. [Figure taken from Riordan (2010)].

Measurements of G_E^n at high Q^2 also help us to understand the symmetry structure of nucleon electromagnetic form factors. Two symmetries play a crucial role: (1) relativistic invariance, which fixes the form of the nucleon current and hence the form of the form factors; and (2) isospin invariance, which gives relations between neutron and proton form factors. While relativistic invariance is expected to be exact, isospin invariance is not exact; however, it is expected to be only slightly broken in a realistic theory of the strong interaction. Isospin invariance leads to the introduction of isoscalar, F_{1S} and F_{2S}, and isovector, F_{1V} and F_{2V}, form factors, and hence to relations among proton and neutron form factors. The observed Sachs form factors, G_E^p and G_E^n, can be obtained from the relations:

$$G_E^p = F_1^p - \tau F_2^p = (F_{1S} + F_{1V}) - \tau (F_{2S} + F_{2V}) \quad (2)$$

$$G_E^n = F_1^n - \tau F_2^n = (F_{1S} - F_{1V}) - \tau (F_{2S} - F_{2V}) \quad (3)$$

where F_1 and F_2 are the Dirac and Pauli form factors. As a consequence of the two-term structure of Eqs. (2,3), with the second term being multiplied by $-Q^2/4M^2$, G_E^p and G_E^n may have zeros at some value of Q^2, depending on the relative sign of the two terms. In addition to the separation into isoscalar and isovector form factors, one can also decompose the proton and neutron form factors into their up quark and down quark contributions, if one negelcts the strange quark contributions which have been shown to be small. Such a comparison is presented in Figure 5, which shows the ratio of down to up quark contributions to both F_1 and F_2.

2.3 Better Understanding of Effects of Relativistic Quarks

Another motivation for measuring G_E^n at higher Q^2 is to obtain a better understanding of effects of relativistic quarks. In the Light Front Cloudy Bag Model (LFCBM) of Miller (2002), the nucleon is modeled as a relativistic system of three bound constituent quarks immersed in a cloud of pions. The pionic cloud is important for understanding low-momentum transfer physics, whereas the quarks dominate at high values of Q^2. The LFCBM predicts that the contribution to G_E^n from the relativistic quarks exceeds the Galster parameterization, as shown in Fig. 6 (top panel); and that the relativistic quarks make the main contribution to G_E^n at high Q^2, as shown in Fig. 6 (bottom panel).

It is not just the improved lever arm that makes high Q^2 measurement highly desirable. Many models treat only the three constituent quarks, and thus do not expect to do a good job of reproducing the data in the lower Q^2 region where pion cloud effects are important. At low Q^2, this makes G_E^n a unique way to examine the pion cloud effects, but it cannot provide strong tests of the models of nucleon structure that do not explicitly include these effects. At high Q^2 values, the proposed measurements of G_E^n will provide a complete set of elastic form factor measurements in the high Q^2 region where pion cloud effects are expected to be small, and where models that can provide reasonable results for the other form factors make wildly varying predictions for G_E^n. In this region, G_E^n takes on another important role, as it is sensitive to the difference in the spatial distribution of positive and negative charge in the neutron, and thus uniquely probes the difference between the up and down quark distributions in the quark core of the nucleon.

2.4 Extraction of the detailed charge distribution of the neutron

Measurements of G_E^n at high Q^2 provide additional information on the charge distribution of the neutron. Because the neutron has no net charge, these distributions directly relate to the difference between the spatial distributions of up and down quarks (assuming the strange quark contributions to be small). In the Infinite Momentum Frame, these distributions can be extracted without the model-dependent boost corrections required to extract the rest frame distributions [Miller 2007]. A recent extension of this analysis which includes an evaluation of the uncertainty in the transverse charge density [Venkat 2010] suggests that data beyond 4 $(\mathrm{GeV/c})^2$ is needed to extract reliable densities for the proton, with coverage to 9 $(\mathrm{GeV/c})^2$ being sufficient to make precise extractions of the density down to very small transverse distance. The requirements for the neutron should be similar, yielding a dramatically improved extraction of the transverse charge density with precise measurements up to 6.9 GeV^2.

2.5 Comparisons to Lattice QCD

J. Negele at MIT has been leading a major effort to use lattice QCD to understand the structure and interaction of hadrons. Fundamental lattice calculations are becoming available to solve QCD, the field theory of quarks and gluons. Currently, lattice calculations are limited by computer power; however, increased computing power is becoming available. Lattice QCD calculations are fundamental, whereas various model calculations are not. Lattice QCD has made impressive strides recently, with rigorous methods for separating hard and soft contributions and recent methods for extrapolation to the chiral limit for light quarks using explicit representations of nonanalytic contributions. In recent years, lattice calculations have entered the regime of precision calculations of selected properties. Computer resources and theoretical developments

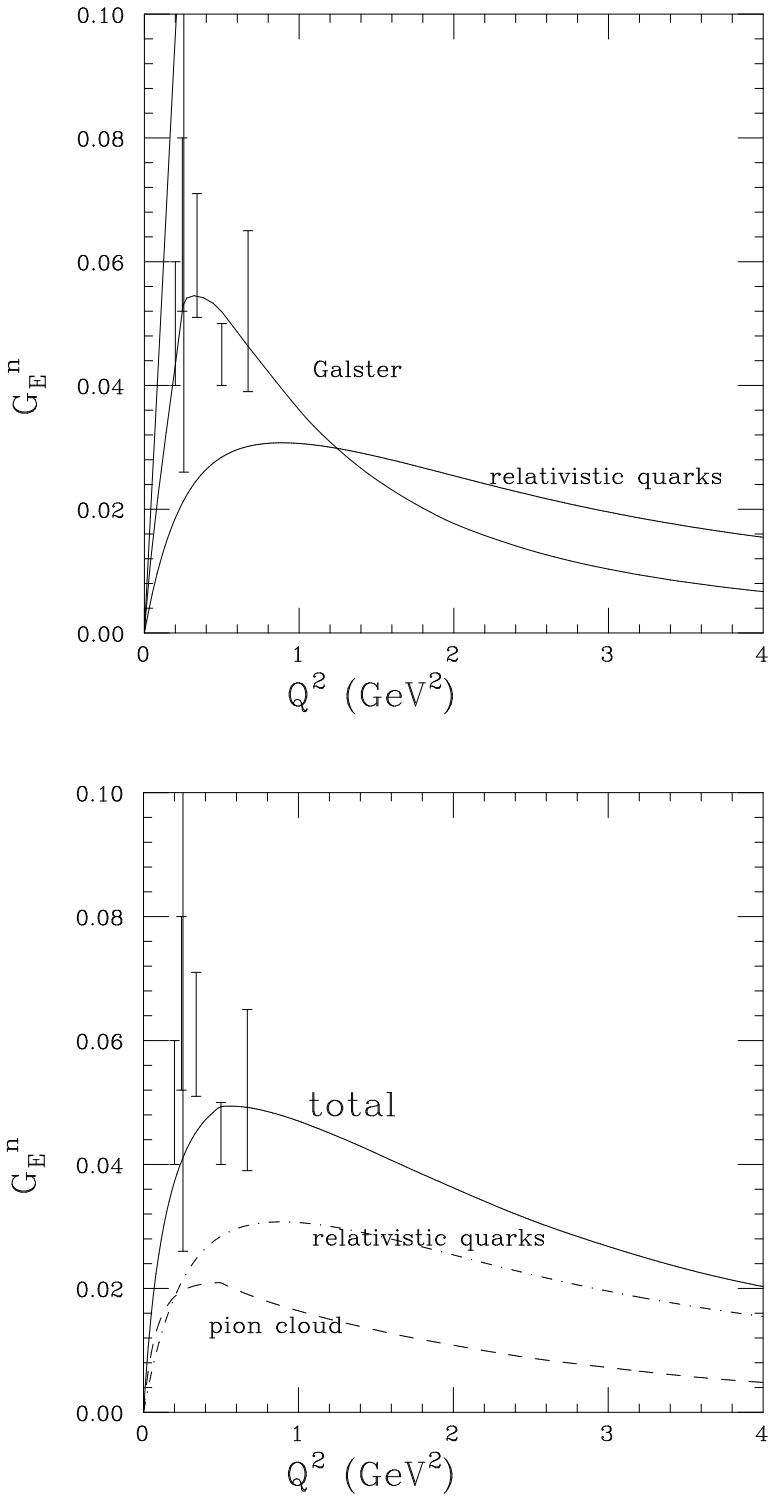

Figure 6: Calculation of G_E^n by Miller (2002): relativistic quarks contribution (top panel) and total LFCBM calculation (bottom panel). [Figure taken from Miller (2002).]

now permit calculations at light enough quark masses that many quantities can be extrapolated to the physical quark mass using chiral perturbation theory. Edwards et al. (2006) calculated the nucleon axial charge from first principles with 6.8% errors and in agreement with experiment. Recently, Hagler et al. (2007) calculated a range of generalized form factors related to generalized parton distributions. One particularly nice result is the contribution of the quark spin and of the quark orbital angular momentum to the total spin of the nucleon. The chiral extrapolations agree well with the recent Hermes analysis. Alexandrou et al. (2006) published results on the isovector electromagnetic form factors, obtained in quenched and unquenched lattice QCD studies, out to Q^2 values of ~ 2 (GeV/c)^2. The unquenched (quenched) calculations employed lattice spacings of 0.08 fm (0.09 fm), and quark masses corresponding to pion masses down to about 380 MeV (410 MeV). An interesting finding reported here (subject to the numerous caveats concerning extrapolations to the continuum limit, and the chiral extrapolation) was that both the unquenched and quenched results were higher than the experimentally extracted isovector form factors, with the deviations largest for the electric isovector form factor. The authors noted that this disagreement was puzzling and warranted further studies with finer lattice spacings.

The present state of the art of lattice calculations has some caveats: (1) Currently, a class of Feynman diagrams, called "disconnected diagrams" are ignored. They are believed to be small, but are roughly two orders of magnitude more expensive to calculate than the connected diagrams that are included at present. These diagrams cancel out of isovector quantities, which therefore are the most reliable quantities to calculate at present. Negele et al. [private communication (2007)] hope to publish their first results of disconnected diagrams soon. (2) Because current lattice spacings of ~ 0.1 fm make it unrealistic to calculate form factors at $Q^2 = 4$ (GeV/c)^2, the calculations generally go only up to $Q^2 = 2$ (GeV/c)^2. The next round will treat finer lattice spacings, which should permit reaching $Q^2 = 4$ (GeV/c)^2.

2.6 Better Understanding of Electron Scattering Data From Nuclei

In their paper on electron scattering from nuclei, Drechsel and Giannini (1989) state (on page 1109) that *"All calculations of nuclear electromagnetic properties suffer from the poor knowledge of G_E^n."* As Q^2 increases, the values of G_E^p, the electric form factor of the proton, approach the values of G_E^n, represented by the modified Galster parameterization. Plotted in Fig. 7 (top panel) as a function of Q^2 are the neutron electric form factor for the modified Galster parameterization, and the proton electric form factor points measured in JLab E93-027 and E99-007. The measured G_E^p points have been fitted with the following parameterization:

$$G_E^p = G_D\,[1 - 0.14(Q^2 - 0.30)] \quad (Fit\ \ to\ \ Hall\ A\ \ FPP\ \ Measurements) \tag{4}$$

with

$$G_D\ \equiv\ (1 + Q^2/0.71)^{-2} \qquad (Dipole) \tag{5}$$

The magnitude of G_E^n is not insignificant compared to G_E^p in the Q^2 region above about 2 (GeV/c)^2. The value of G_E^n from the modified Galster fit exceeds the value of G_E^p above $Q^2 \sim$ 4.4 (GeV/c)^2; accordingly, the isovector electric form factor would become negative in this Q^2 region. As shown in Fig. 7, the most recent model of Bijker and Iachello (2004) predicts that the isovector electric form factor becomes negative at a Q^2 of about 3 (GeV/c)^2; whereas the model of Miller et al. (2002) predicts a crossover at $\sim$4.3 (GeV/c)^2. The isovector form factor [i.e., a difference between G_E^p (E93-027/E99-007) and G_E^n (New Fit from E93-038)] is plotted in the bottom panel of Fig. 7. The G_E^p data measured in E93-027 turned out to be a surprise —

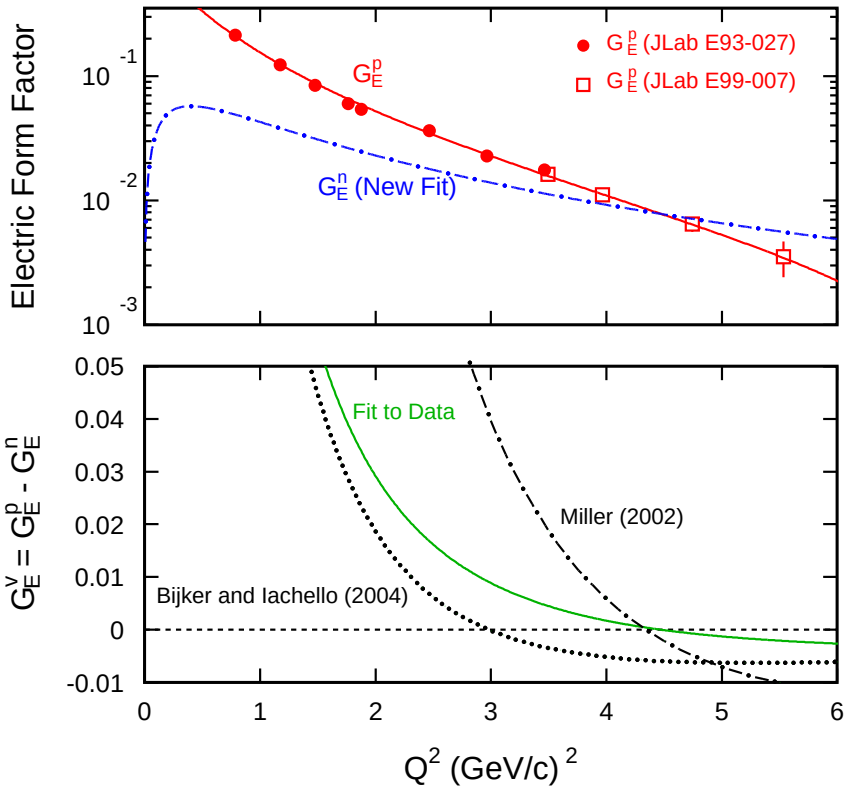

Figure 7: Proton, neutron, and isovector form factors as a function of Q^2. The solid line through the G_E^p points in the top panel is a parameterization from Eq. (4) for G_E^p. Bottom panel: the solid line is a difference of the G_E^p and G_E^n parameterizations from the top panel, the dotted line is a calculation by Bijker and Iachello (2004), and the dash-dotted line is a calculation by Miller et al. (2002).

falling faster with Q^2 than expected from the global analysis of earlier SLAC data. The nature of the decrease of G_E^n with Q^2 may be a surprise also.

Because the isovector electric form factors of nuclei are proportional to the difference $G_E^p - G_E^n$ (and the isoscalar electric form factors are proportional to the sum $G_E^p + G_E^n$), the value of G_E^n is needed for the understanding of electron scattering experiments that probe electric structure functions at high momentum transfer. The ratio of the isoscalar cross section to the isovector cross section depends sensitively on the value of G_E^n:

$$\frac{\sigma_{isoscalar}}{\sigma_{isovector}} = \left(\frac{G_E^p + G_E^n}{G_E^p - G_E^n} \right)^2 \tag{6}$$

This ratio is plotted in Fig. 8 as a function of Q^2. This ratio is unity if $G_E^n = 0$; however, this ratio is about 4.4 at $Q^2 = 1.45$ (GeV/c)^2 and about 100 at $Q^2 = 4.0$ (GeV/c)^2 if G_E^n continues to follow the modified Galster parameterization and if G_E^p follows Eq. (4). A better knowledge of G_E^n is needed for the interpretation of electron scattering from nuclei at high momentum transfer. This knowledge is needed for the analysis of few-body data from measurements at Jefferson Lab, which are in the Q^2 range above the existing G_E^n data.

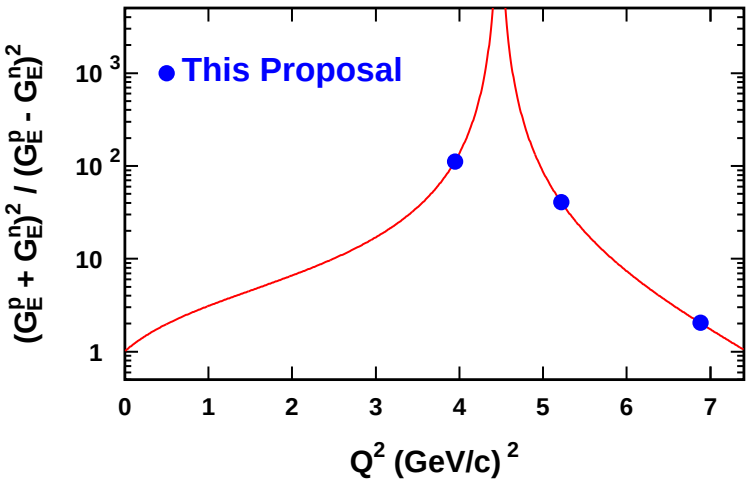

Figure 8: The ratio of isoscalar and isovector cross-sections [Eq. (6)] as a function of Q^2. We assume the modified Galster parameterization (New Fit from E93-038) for G_E^n and the parameterization from Eq. (4) for G_E^p.

2.7 Nuclear Physics Corrections and Reaction Mechanism Questions

Figure 9 shows the results from E93-038 for three cases: (1) The triangles are for a point acceptance; (2) the circles are acceptance-averaged PWBA values; and (3) the squares are the acceptance-averaged values based on Arenhoevel's full calculation [including FSI, MEC, and IC]. In E93-038, the nuclear physics corrections [for FSI, MEC, and IC] increased G_E^n over the values obtained with the PWBA model by 5.6, 4.0, and 3.3 percent at $Q^2 = 0.45$, 1.13, and 1.45 (GeV/c)^2, respectively. While the magnitude of the nuclear corrections are expected to continue to decrease with increasing Q^2, the nuclear corrections are more reliable [and most likely smaller] for deuterium than for helium. Arenhoevel [2003] carried out calculations for deuterium for the previously proposed kinematics at $Q^2 = 4.3$ (GeV/c)^2; his results are shown in Fig. 10.

Also, the reaction mechanism is expected to be simpler in deuterium than in helium. In the case of the proton form factor ratio, comparisons of results obtained via the recoil polarization technique with results obtained via the Rosenbluth separation technique have provided strong evidence that two-photon exchange physics can significantly impact elastic electron-proton scattering observables. For the neutron, the TPE corrections are believed to be much smaller, and a negligible correction for the polarization measurements. However, there are other important corrections in the extraction of the neutron form factors from measurements of polarization observables in quasielastic scattering from ^{2}H or ^{3}He.

Given all of these issues, it is important to have precise measurements using ^2H recoil polarization measurements, to ensure that the larger corrections for the ^{3}He measurements can be performed reliably at high Q^2, as these measurements will eventually yield the highest Q^2 results. There are suggestions of a mismatch between the previous recoil polarization and high Q^2 polarized target measurements, accentuated in the flavor decomposition of F_1 and F_2 (Fig. 5). One possible difference is the larger corrections for nuclear effects required in the extraction from ^{3}He, emphasizing the need for careful cross-checks.

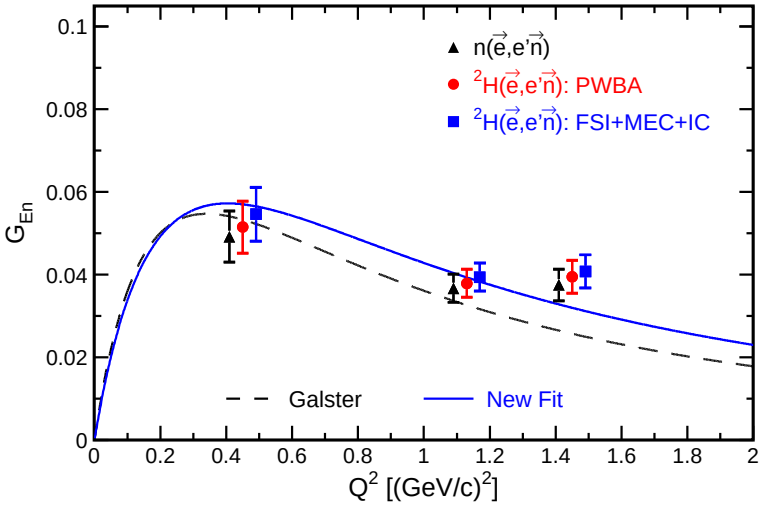

Figure 9: Comparison of the final results for G_E^n extracted from analyses assuming $n(\vec{e}, e'\vec{n})$ elastic scattering and a point acceptance (triangles), the acceptance-averaged $^2\mathrm{H}(\vec{e}, e'\vec{n})^1\mathrm{H}$ Arenhövel PWBA model (circles), and the acceptance-averaged $^2\mathrm{H}(\vec{e}, e'\vec{n})^1\mathrm{H}$ Arenhövel FSI+MEC+IC model (squares). The error bars shown are the quadrature sum of the statistical and systematic errors.

3 Theoretical Background: Extraction of G_E^n

For the proton, the form factors have typically been performed by measuring the elastic electron–proton cross section over a range of angles, i.e., performing a Rosenbluth separation. The fundamental limitation of the Rosenbluth separation technique is that is it sensitive to a combination of the electric and magnetic form factors, $\tau(G_M^n)^2 + \varepsilon(G_E^n)^2$, where $\tau = Q^2/4M^2$, and ε is the virtual photon polarization parameter, which is sensitive to the electron scattering angle. At fixed Q^2, G_E^n is determined by measuring the variation of the cross section with scattering angle (ε). For the neutron, $(G_E^n)^2 \ll (G_M^n)^2$, and so the cross section has little sensitivity to G_E^n, and measurements would be difficult even if a free neutron target were available.

The lack of free neutron targets meant that the electron–neutron cross section had to be determined from quasielastic scattering on a deuteron target. Subtraction of the contribution from the proton in the deuteron introduced large uncertainties. In addition, there are large model-dependent corrections and uncertainties due to uncertainties in the theoretical description of the deuteron, mostly from final-state interactions (FSI) and meson-exchange currents (MEC). In the Q^2 region from 1.75 to 4.00 (GeV/c)^2, Lung et al. (1993) reported measurements from SLAC-NE11 of quasielastic $e - d$ cross sections at forward and backward angles which permit a Rosenbluth separation of G_E^n and G_M^n at $Q^2 = 1.75$, 2.50, 3.25, and 4.00 (GeV/c)^2. Although Lung et al. (1993) stated that their data from SLAC-NE11 were consistent with $(G_E^n)^2 = 0$ for $1.75 < Q^2$ (GeV/c)$^2 < 4.00$, these data appear consistent also with the modified Galster parameterization. The NE11 error bars do not permit distinguishing between $G_E^n = 0$ and the Galster parameterization.

In contrast to the Rosenbluth separation method, measurements utilizing polarization observables are sensitive to the ratio G_E^n/G_M^n; therefore, knowledge of G_M^n taken from cross section measurements can be combined with polarization measurements to make precise extractions of both G_E^n and G_M^n. In addition, this technique allows an experimental determination of the sign of G_E^n, which is impossible in the Rosenbluth separation (as only $(G_E^n)^2$ appears). This is

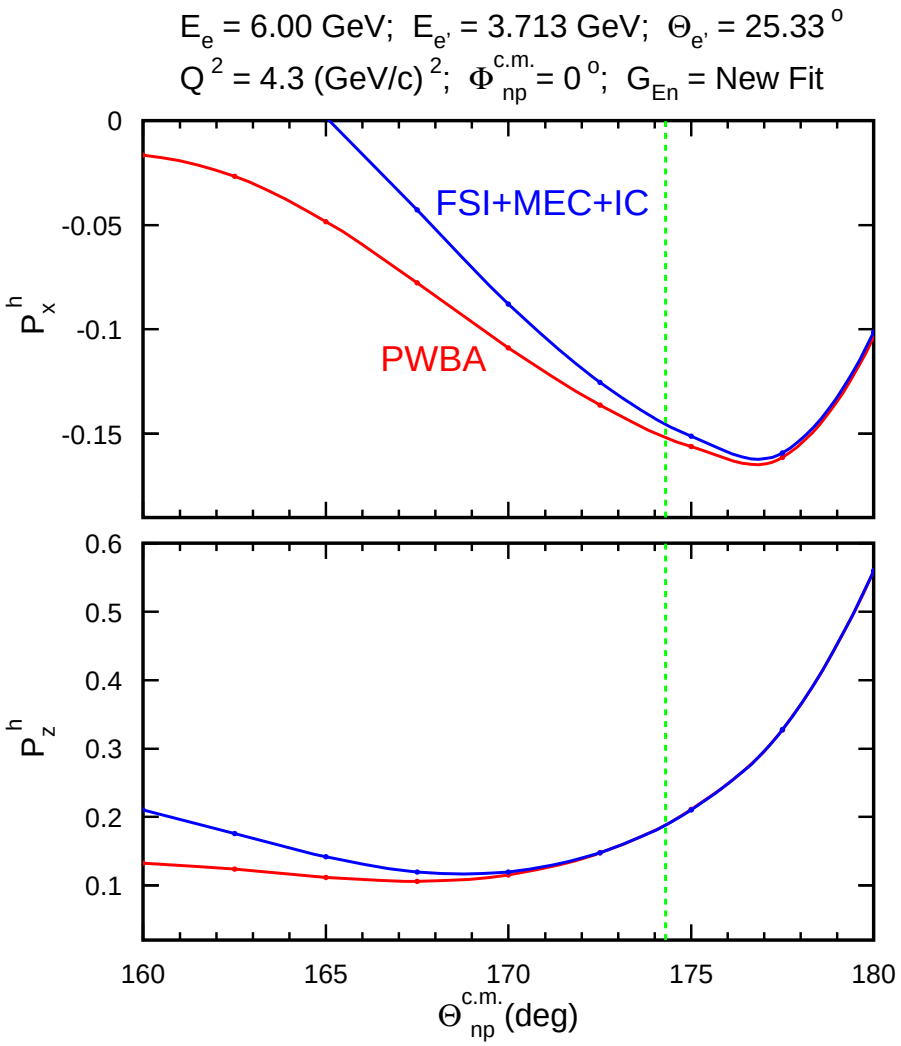

Figure 10: Comparison of Arenhoevel's PWBA and FSI+MEC+IC calculations of P_x^h and P_z^h at the previously proposed kinematics of $Q^2 = 4.3$ (GeV/c)^2.

another nice feature of the polarization transfer technique - especially in view of the fact that nothing is known about the sign of G_E^n at high Q^2.

The measurements still require scattering from a neutron in a nucleus, but the corrections due to nuclear effects are much smaller than for the case of unpolarized scattering. Arenhoevel (1987) calculated the effect of the electric form factor of the neutron on the polarization transfer in the $d(\vec{e}, e'\vec{n})p$ reaction in the quasifree region, where the deuteron serves as a neutron target while the proton acts mainly as a spectator. Using a nonrelativistic theory and a realistic nucleon-nucleon potential, Arenhoevel found that the sideways polarization of the recoil neutron $P_{S'}$, which vanishes for coplanar kinematics and unpolarized electrons, is most sensitive to G_E^n for neutron emission along the momentum-transfer direction in the quasifree case. Using the parameterization of Galster et al. (1971) for G_E^n, Arenhoevel's calculation indicates that even away from the forward-emission direction (with respect to the direction of the momentum transfer $\vec{q}$), the increase in the sideways polarization of the neutron $P_{S'}$ is small for $G_E^n = 0$, but increases when G_E^n is switched on, and that this increase prevails up to a neutron angle of nearly 30^o measured with respect to $\vec{q}^{\,c.m.}$ in the center-of-mass system. In the forward direction

with respect to $\vec{q}^{\,c.m.}$, Arenhoevel found also that the neutron polarization $P_{S'}$ is insensitive to the influence of final-state interactions (FSI), meson-exchange currents (MEC), and isobar configurations (IC), and that this lack of sensitivity holds again up to an angle of nearly 20^o away from the forward direction with respect to $\vec{q}^{\,c.m.}$, which corresponds to a laboratory angle of about a few degrees away from the forward direction with respect to the $\vec{q}^{\,lab}$. Arenhoevel also studied the influence of different deuteron wave functions on the sideways neutron polarization $P_{S'}$. His results for quasifree kinematics (i.e., for neutron emission along $\vec{q}$) show almost no dependence on the deuteron model. The Arenhoevel calculation shows that dynamical uncertainties are very small. Finally, Beck and Arenhoevel (1992) investigated the role of relativistic effects in the electrodisintegration of the deuteron for quasifree kinematics. They found that the dependence on the parameterization of the nucleon current in terms of Dirac-Pauli or Sachs form factors is reduced considerably by inclusion of the relativistic contributions. Also, for quasifree emission, Arenhoevel (2002) demonstrated that $P_{L'}$ is insensitive to FSI, MEC, IC, and to theoretical models of deuteron structure.

Rekalo, Gakh, and Rekalo (1989) used the relativistic impulse approximation to describe the polarization effects sensitive to G_E^n in deuteron electrodisintegration. In the deuteron quasielastic peak, the neutron polarizations calculated in the relativistic approach agree with the results of Arenhoevel (1987). A later study by Mosconi, Pauschenwein, and Ricci (1991) of nucleonic and pionic relativistic corrections in deuteron electrodisintegration does not change the results of Arenhoevel. Laget (1990) investigated the effects of nucleon rescatterings and meson-exchange currents on the determination of the neutron electric form factor in the $d(\vec{e},e'\vec{n})p$ reaction. He concluded that a measurement of the sideways polarization of the neutron appears to be the most direct way to determine the neutron electric form factor. He concluded also that in quasifree (colinear) kinematics, the neutron polarization in the exclusive reaction is equal to the value expected in the elementary reaction $n(\vec{e},e'\vec{n})$ and that corrections from final-state interactions and meson-exchange currents are negligible above $Q^2 = 0.30$ (GeV/c)^2, but that these corrections become sizeable below this momentum transfer; however, Herberg et al. (1999) found that (even in the quasifree peak) corrections for FSI in $d(\vec{e},e'\vec{n})p$ measurements at Mainz amounted to (8±3)% for $Q^2 = 0.34$ (GeV/c)^2 and (65±3)% for $Q^2 = 0.15$ (GeV/c)^2 of the value unperturbed by FSI. In E93-038, we found that the nuclear physics [FSI+MEC+IC] corrections were small and decreased with increasing Q^2. The nuclear physics corrections increased G_E^n over the value obtained with the PWBA by only 5.6, 4.0, and 3.3 percent at $Q^2 = 0.45$, 1.13, and 1.45 (GeV/c)^2, respectively. These corrections were based on the model of Arenhoevel et al. (1988).

4 Description of the Experiment

4.1 Review of Recoil Polarimetry Technique

The proposed technique will extract values for the neutron electric to magnetic form factor ratio, G_E^n/G_M^n, from measurements of the neutron's recoil polarization in the quasielastic scattering of longitudinally polarized electrons from unpolarized neutrons in deuterium. In the one-photon-exchange approximation, the transverse and longitudinal components of the neutron's recoil polarization (defined in the electron scattering plane relative to the neutron's momentum) are of the form [Arnold (1981)]:

$$\begin{aligned} P_t &= -2P_e G_E^n G_M^n K_t, \\ P_\ell &= 2P_e {G_M^n}^2 K_\ell, \end{aligned} \tag{7}$$

where P_e is the electron beam polarization, and K_t and K_ℓ are electron kinematic factors.

Both recoil polarization components $P_t \propto -G_E^n G_M^n$ and $P_\ell \propto {G_M^n}^2$ are accessed via a secondary analyzing reaction in our neutron polarimeter configured to measure an up-down scattering asymmetry. Transport through a vertical magnetic dipole field located ahead of the polarimeter results in a precession of the recoil polarization vector through some angles χ, leading to a scattering asymmetry $\xi(\chi)$ which is sensitive to a mixing of P_t and P_ℓ. With another measurement of the scattering asymmetry ξ_- for a precession through an angle $-\chi$, the ratio of G_E and G_M is given by

$$g \equiv \left(\frac{G_E}{G_M}\right) = K_R \, tan(\chi) \, \frac{(\eta+1)}{(\eta-1)} \tag{8}$$

where the asymmetry ratio

$$\eta \equiv \frac{\xi_-}{\xi_+} = \frac{P_-^x}{P_+^x} \tag{9}$$

and K_R is a kinematic function that is determined by the electron scattering angle θ_e and four-momentum transfer Q^2 in the d($\vec{e}$,e'$\vec{n}$)p reaction.

A significant advantage of this technique for measuring the ratio of the two scattering asymmetries is that the scale and systematic uncertainties are minimal because the relative uncertainty in the analyzing power of the polarimeter does not enter in the ratio. The same is true for the beam polarization P_L because, as demonstrated in E93-038, P_L does not change much during sequential measurements of ξ_+ and ξ_-.

4.2 Kinematics and Neutron Polarimeter

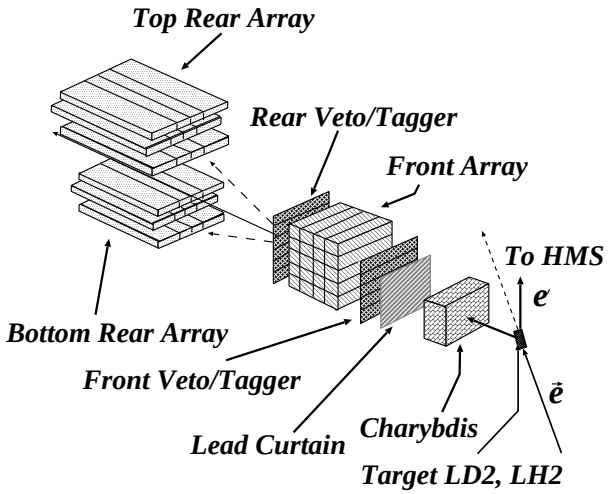

Figure 11: Schematic diagram of the experimental arrangement in E93-038.

The experimental arrangement is similar in principle to the one used in E93-038 (shown in Fig. 11). The scattered electron from the d($\vec{e}$,e'$\vec{n}$)p reaction is detected with the Super High Momentum Spectrometer (SHMS) in coincidence with the recoil neutron. A polarimeter detects the recoil neutron and measures the up-down scattering asymmetry from the projection of the polarization vector on the transverse axis. A dipole magnet in front of the polarimeter precesses the neutron polarization vector through an angle $\pm\chi$ to permit measuring the scattering asymmetry $\xi_\pm$ from the polarization vector component on the transverse (or sideways) direction. For

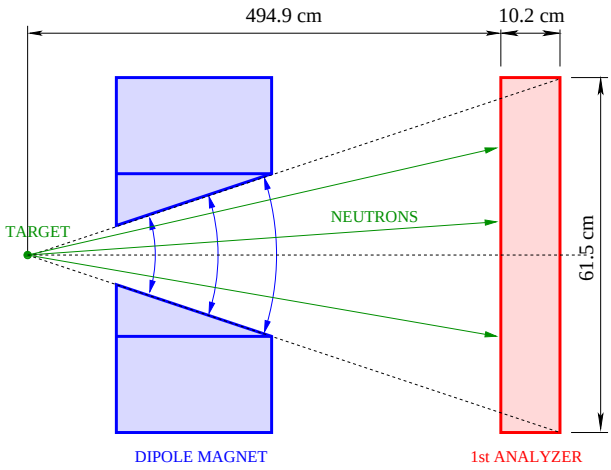

Figure 12: Tapered poles of Dipole Magnet (side view). [Drawing is not to scale to emphasize the vertical dimension.]

a total data-acquisition time T, the time fractions for measuring ξ_+ and ξ_- are optimized to minimize the statistical uncertainty in g.

In E93-038, we used the CHARYBDIS dipole magnet with an 8.25-inch gap and 2-inch field clamps. The 8.25-inch gap was large enough to illuminate fully the 0.5-m high by 1-m wide front array of the E93-038 polarimeter. To illuminate fully the analyzer arrays of the proposed polarimeter, we plan to use the dipole magnet with the tapered gap between the magnet poles (see Fig. 12). Such a configuration of the gap permits minimizing the current in the magnet that is needed to reach the desired field integral. Other advantages of such a gap are:

1. The magnetic field in the gap is almost perpendicular to the momentum of all neutrons emitted from the target in to the analyzer arrays;

2. The dipole magnet poles provide additional collimation to protect the polarimeter top/bottom arrays from the direct particles from the target.

The precession angle χ is the angle of rotation of the polarization vector after traversing the magnetic field. The neutron spin precession angle χ is given by

$$\chi \;=\; -\frac{ge}{2M_p c\beta_n}\int B\Delta l \;=\; \frac{1.913e}{M_p c\beta_n}\int B\Delta l \qquad (10)$$

where $g/2$ = -1.913.

Table 1 lists the kinematic conditions and the $B\Delta l$ required to precess the neutron polarization vector through χ degrees. The accelerator should be able to deliver a beam polarization of 80% at any energy (see Fig. 32). The range of reasonable angles of neutron spin precession is limited on the small-angle side by the requirement to have the magnetic field in the dipole magnet strong enough to deflect a significant part of the quasielastic protons away from the analyzer arrays of the polarimeter, and on the large-angle side by the fact that the statistical uncertainty increases with precession angle χ, as shown in Fig. 25. Any precession angle χ between 130 and 160 degrees yields an excellent figure of merit; the precession angles that correspond to the field integral of 4.0 Tm were chosen.

To increase the efficiency of the neutron polarimeter and access neutron scattering at relatively small angles (where the maximum of analyzing power is located, see Fig. 13), we propose

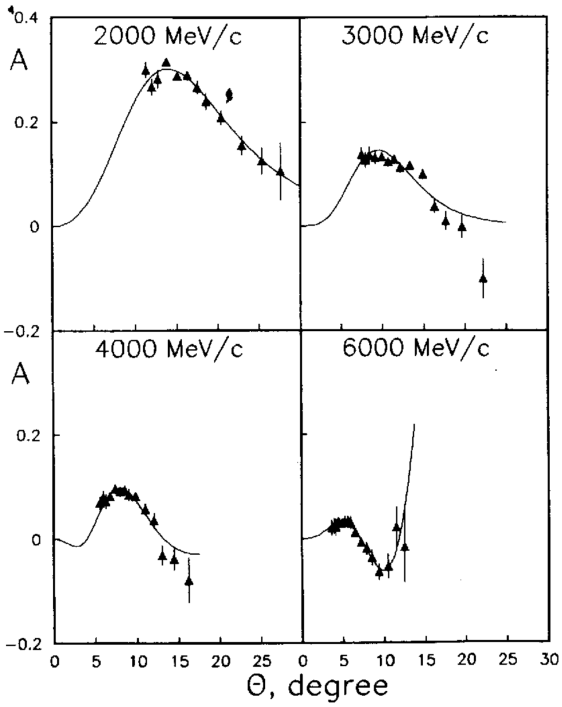

Figure 13: Analyzing power as a function of neutron scattering angle from the np elastic scattering data (figure from [Ladygin (1999)]).

an updated version of the polarimeter (see Fig. 14) to be used for these measurements [Semenov (2010)]. At the Q^2 values proposed herein, the higher energy of the quasielastic neutron from the target allows detection of the recoil proton from the neutron scattering in the analyzer of the neutron polarimeter (see Fig. 15) instead of detection of the scattered neutron as it was in the E93-038. Updated polarimeter consists of 6 sections; each section consists of one vertical 10-cm-thick layer of analyzer scintillation detectors and top and bottom 1-cm-thick (ΔE-arrays and 10-cm-thick E-arrays to identify the recoil proton from the neutron scattering events in the analyzer. Vertical dimensions of the sections are chosen to fit the solid angle visible from the target through the polarimeter collimator: 1st and 2nd sections have 60-cm-high analyzers, 3rd and 4th sections have 80-cm-high analyzers, and the last 2 sections have 100-cm-high analyzers.

The polarimeter now consists of 48 detectors in the analyzer arrays, 39 ΔE-detectors and 40 E-detectors in each of two top/bottom arrays. A double layer of 12 veto/tagger detectors is located ahead of the first analyzing array. The thin scintillator detectors of ΔE-arrays are located in between the top/bottom E-arrays and the analyzing arrays; analysis of the amplitudes of signals from these detectors together with the signal amplitudes from the detectors of the top/bottom E-arrays will provide ΔE-E identification of the recoil protons (in addition to the measurements of TOF between the analyzer and top/bottom array detectors, see Fig. 16). To permit high luminosity, the dimensions of each of the detectors in the analyzing and E-arrays are 10 cm$\times$10 cm$\times$100 cm; the dimensions of veto detectors and the detectors in the ΔE-arrays are 10 cm$\times$1 cm$\times$106 cm. The top/bottom arrays detectors are shielded from the direct path of neutrons from the target.

In our previous proposal (submitted by PAC35), we estimated the polarimeter efficiency using elastic *np* cross sections and simulated polarimeter efficiency of collection of recoil protons from quasielastic neutron scattering in the polarimeter analyzer; that was a definite underestimation

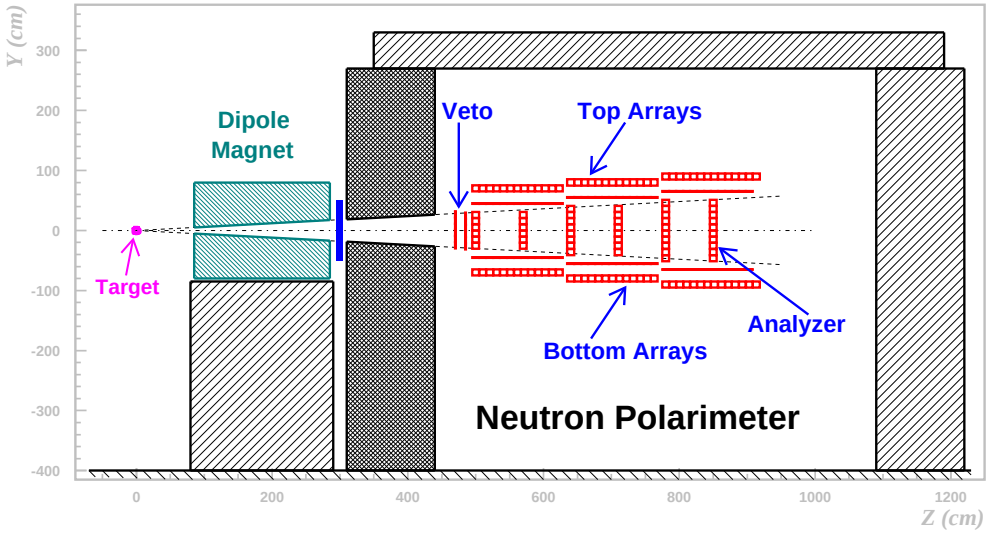

Figure 14: Neutron polarimeter to be used in the measurements.

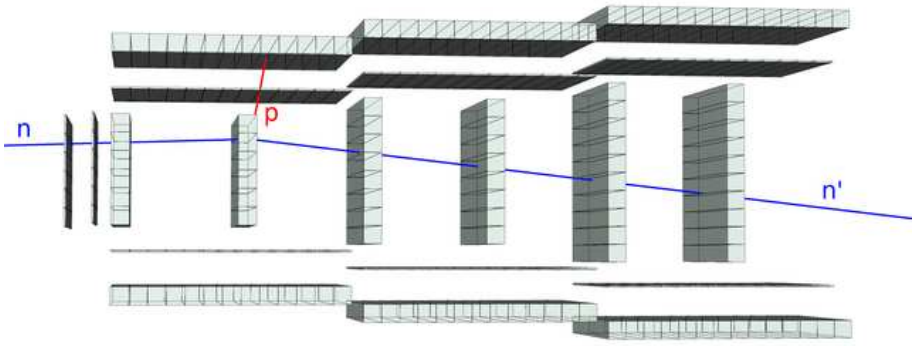

Figure 15: Example of neutron scattering in the polarimeter. Event from FLUKA 2008.3b.2 is visualized using SimpleGEO program [Theis (2006)].

of the real polarimeter efficiency. In the polarimeter simulation for this proposal, we directly sent the flux of quasielastic neutrons on the polarimeter model in to the FLUKA 2008.3b.2 program [Fasso et al. (2001)], recorded event-per-event energy depositions in the detectors, applied analysis cuts and selected the events of interest, and estimated the polarimeter efficiency. For each of Q^2 kinematics, the neutron flux had angular distribution according to correspondent MCEEP simulation with p_{rec} $\leq$250 MeV/c. The numerator in the efficiency formula is the number of events that pass the set of criteria:

1. At least one hit (energy deposition $\geq$ 1MeV) in some detector in the analyzer and an energy deposition of $\geq$ 1MeV in some detectors in the ΔE- and E-arrays (both top or both bottom) in the same section.

2. No hits in the analyzers in the previous (upstream) sections to avoid counting of secondary scatterings in the polarimeter.

3. Total energy in the analyzer detectors in the section of interest should be more than 4 MeV; total energy deposition in the E-array of interest should be more than 5 MeV.

Four-Momentum Transfer, Q^2 (GeV/c)^2	3.95	5.22	6.88
Beam Energy, E_0 (GeV)	4.4	6.6	11.0
Electron Scattering Angle, θ_e (deg)	36.53	26.31	16.79
Scattered Electron Momentum, P_e' (GeV/c)	2.288	3.815	7.330
Neutron Scattering Angle, θ_n (deg)	28.0	28.0	28.0
Neutron Momentum, P_n (GeV/c)	2.901	3.602	4.511
Neutron Kinetic Energy, T_n (GeV)	2.110	2.783	3.668
Flight Path, x (m)	5.0	5.0	5.0
Precession Angle, χ (deg)	147.3	144.8	143.1
Field Integral to Precess Neutron Spin through χ Degree, $B\Delta l$ (Tm)	4.0	4.0	4.0

Table 1: Kinematic conditions at a neutron scattering angle of 28.0^o. Also listed is the dipole magnet field integral $B\Delta l$ required to precess the neutron polarization vector.

4. Total energy deposition in the analyzer+ΔE+E detectors in the section of interest should be $\geq$ 50 MeV (viz., a little bit more than the minimum ionizing particle (MIP) crossing two 10-cm-thick detectors).

5. Top/Bottom asymmetry of energy depositions in the section of interest (for example, if we have "good" energy depositions in the bottom dE- and E-arrays, the total energy deposition in the top arrays should be at least 20 times less than in the bottom ones. And vice versa...) This criterion helps suppress inelastic interactions and select recoil protons from elastic and quasielastic scatterings of neutrons in the polarimeter analyzer.

6. Because the analyzing power is concentrated in the range of the neutron scattering angles of 4-25 degrees (Fig. 13), we applied correspondent cuts on the "recoil proton" scattering angle (viz., 45.3-81.6 degrees at Q^2 = 3.95 (GeV/c)^2, 40.8-80.2 degrees at 5.22 (GeV/c)^2, and 36.0-78.3 degrees at (GeV/c)^2).

Fig. 17 shows the efficiencies for each of the sections, the total polarimeter efficiencies are 4.01%, 5.00%, and 5.85% at Q^2 = 3.95, 5.22 and 6.88 (GeV/c)^2, respectively. Fig. 16 shows the ΔE-E plots for the selected events with the MIP spot (viz., about 2.5 MeV for ΔE and about 25 MeV for E array; about 20% of total statistics that contains both secondaries from inelastics and "fast" protons from quasielastic scatterings) and well visible "angled" band for protons.

Simulation shows that high segmentation of the scintillator detectors in the polarimeter will allow one to reconstruct reliably the polar angle of the recoil proton with an accuracy of 5-6 degrees that will permit controlling the angle of the neutron scattering in the analyzer array with an accuracy of 1.5-2 degrees (to maximize the FOM) and practically eliminate the loss of statistics associated with accidental coincidences of the quasielastic neutrons and detected background particles in the analyzer arrays.

The 10-cm lead curtain ahead of the polarimeter is required to attenuate electromagnetic radiation and also to reduce the flux of charged particles incident on the polarimeter. The curtain thickness is chosen to maintain an acceptable singles rate at a beam current of 80 μA (see description of the simulation in Section 4.7). *If we find during the experiment that the singles rates in the analyzer arrays are low enough or too high, we will decrease or increase the thickness of the lead curtain, respectively.* In E93-038, the singles counting rate in one of the detectors decreased markedly when the thickness of the Pb was increased from 5 cm to 10 cm;

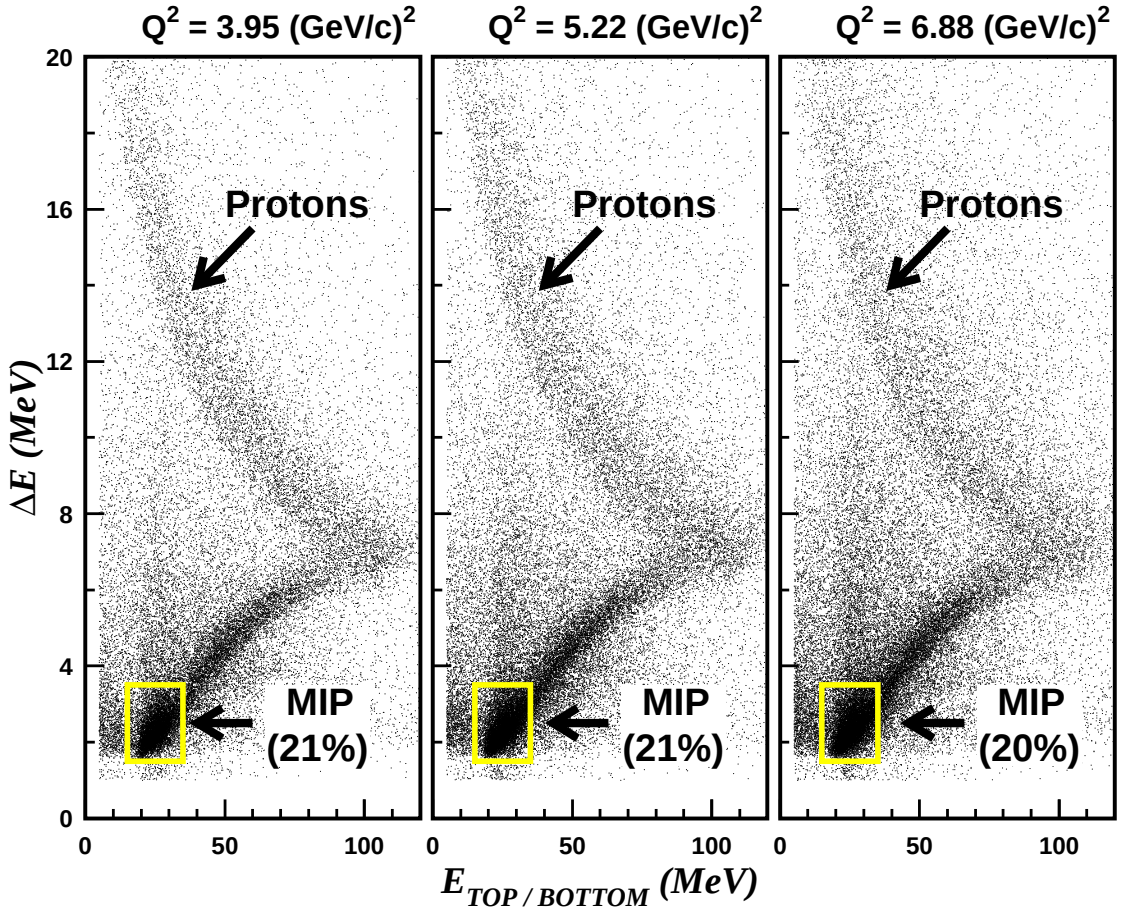

Figure 16: ΔE-E identification of the recoil protons from the scattering of quasielastic neutrons in the analyzer arrays. Results of the neutron polarimeter simulations with FLUKA 2008.3b.2. The "angled" band for protons is very well visible. Yellow boxes show the locations of minimum ionizing particles (MIP) that are both secondaries from inelastics and "fast" protons from quasielastic scatterings; the fraction of MIP events is about 20-21% from the total number of events in the plot.

for example, the singles rates in one of the veto detectors (160 cm wide × 11 cm high × 0.64 cm thick) at a distance of about 6.7 m from a 15-cm LD_2 target are plotted in Fig. 18 as a function of the electron beam current at an energy of 884 MeV. For all beam currents, the singles rate is about five times higher with a 5-cm Pb curtain. E93-038 used a 10-cm lead curtain in order to run at higher beam currents. We do not have data with a 5-cm lead curtain at higher beam energies. E93-038 ran with a 10-cm Pb curtain for all these energies.

To measure the false asymmetry or the dilution of the asymmetry from the two-step process $d(\vec{e}, e'\vec{p})n + Pb(\vec{p}, \vec{n})$, we will take data with an LH_2 target. In the second charge-exchange step, the sign of the polarization transferred to the neutron will be opposite to that from the primary $d(\vec{e}, e'\vec{n})p$ process because the sign of the magnetic moment of the proton is opposite to that of the neutron.

4.3 Comparison to PAC34 Polarimeter Design

In our PAC34 proposal, we proposed a polarimeter with a configuration much more like that used in the 6 GeV experiment (Fig. 11). In our estimates for the figure of merit of the detector,

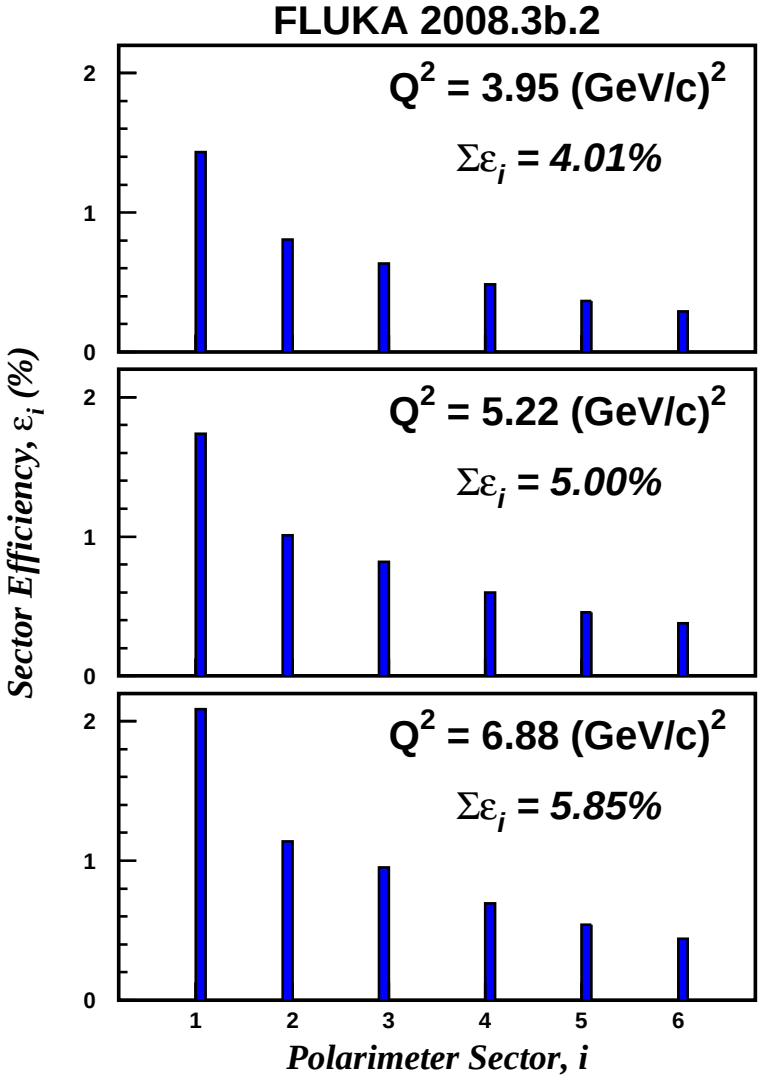

Figure 17: Efficiencies for each of the sections; the total polarimeter efficiencies are 4.01%, 5.00%, and 5.85% at $Q^2 = 3.95$, 5.22 and 6.88 (GeV/c)^2, respectively.

we took measured analyzing power for neutron scattering from CH_2, and extrapolated the peak analyzing power to higher neutron momentum assuming that the neutron analyzing power scaled in the same way as the proton analyzing power. We then assumed that the angular distribution at higher neutron momenta was indentical to that mesured in the previous experiment. While this was a reasonable approximation over some range of momenta, it is not a good approximation when going to significantly higher nuutron momenta. We had some discussions with Charles Perdrisat shortly after the PAC meeting, and determined that the angular distribution was much better represented by a fixed distribution in neutron transverse momentum rather than a fixed distribution in angle. This had two significant consequences on the proposed experiment. First, it meant that it was important to measure rescattered neutron at smaller angles than was assumed in the PAC34 proposal. Second, it yields a significant increase in the figure of merit for the experiment, as the peak in analyzing power moves to smaller scattering angles, where the rescattering cross section is much larger.

The analyzing power measured in the 6 GeV experiment peaked around 18–20 degrees, corresponding to a neutron transverse momentum of 0.45–0.50 (GeV/c). Thus, the original

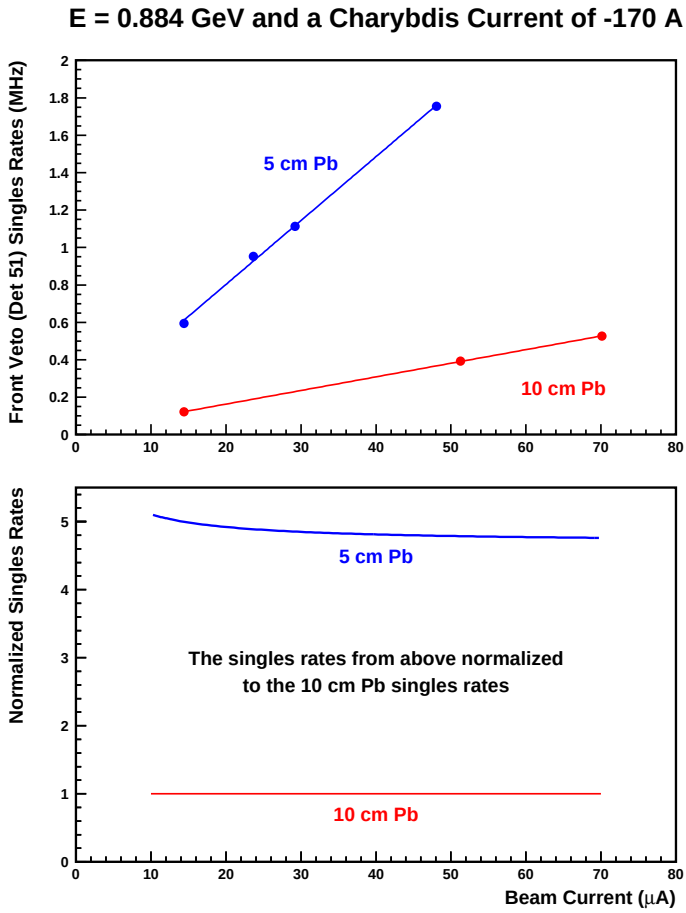

Figure 18: Singles rates for beam energy of 884 MeV and a CHARYBDIS current of -170 A.

polarimeter was designed to have acceptance for scattered neutrons between 10 and 25 degrees. However, a transverse momentum of 0.5 (GeV/c) corresponds to a scattering angle of ≈10 degrees for our Q^2=4 (GeV/c)^2 point, and ≈6 degrees at Q^2=6.9 (GeV/c)^2. Thus, the previous design is not appropriate at these high Q^2 values. The coverage at smaller scattering angles could be improved by moving the rear detection array further back, but if we want to cover neutron angles of 4–10 degrees for the high Q^2 measurement, we need a significantly larger setup, and begin to have trouble measuring the scattering angle reliably, even though the polarimeter was designed to have good reconstruction of the neutron rescattering angle.

However, while the fact that the analyzing power peaks at smaller angles required a redesign of the polarimeter, it also yields a significantly improvement in the potential figure of merit. Instead of peaking around 20 degrees, the analyzing power peaks around 10 degrees for our lowest Q^2 point and 6 degrees for the highest Q^2. Because the cross section is much larger at the smaller scattering angles, the figure of merit of the polarimeter increases with this increase in cross section. This yields an improvement on the scale of a factor of 10, with a larger improvement at higher Q^2 where the peak analyzing power is at smaller angles.

4.4 Analysis Techniques

Extraction of a reliable result for G_E^n from the quasielastic ^{2}H$(\vec{e}, e'\vec{n})^1$H reaction requires the suppression of inelastic events associated with pion production. As discussed in detail in Appendix A of our proposal, quasielastic events are selected via tight cuts on the electron momentum

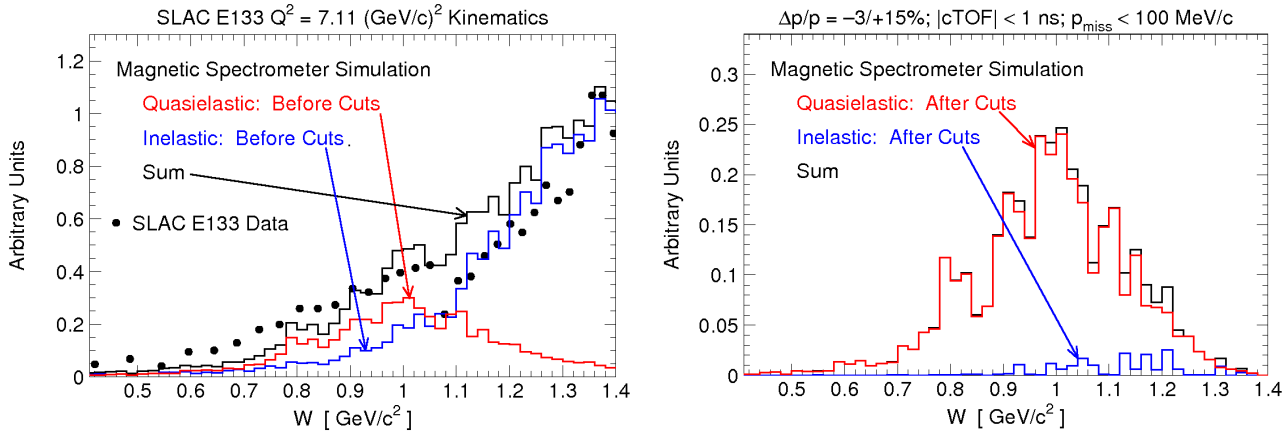

Figure 19: Invariant mass spectra at $Q^2 = 7.1$ (GeV/c)^2 before (left panel) and after (right panel) cuts on the scattered electron momentum, the missing momentum, and an SHMS-NPOL coincidence time-of-flight. Quasielastic and pion-production spectra are simulated separately with GENGEN 2.9 code [Kelly (2000)] and normalized on the invariant mass spectrum at similar kinematics from SLAC E-133 [Rock (1992)]. The inelastic contamination for $W < 1.1$ GeV/c^2 is estimated to be $\sim 3\%$ for $p_{miss} < 100$ MeV/c cut (right panel) and $\sim 8\%$ for $p_{miss} < 250$ MeV/c cut (not shown in figure).

bite $\Delta p/p$, the missing momentum $p_{\rm miss}$, and the electron-neutron coincidence time-of-flight cTOF. Our simulations (assuming the SHMS magnetic spectrometer's projected energy resolution) have indicated that the inelastic contamination in our proposed measurements will be quite small (e.g., see Fig. 19). In contrast, simulations we performed assuming a degraded energy resolution (e.g., such as would result from a calorimetric approach to detection of the scattered electron) indicated that a small inelastic contamination may possibly be achievable, but at the expense of a reduced quasielastic yield (i.e., from broad W distributions).

To extract the physical scattering asymmetry in the polarimeter, we will form time-of-flight spectra between the polarimeter analyzer and top/bottom E-arrays (similar to ΔTOF spectra in E93-038; see Section 5 for details) for the four possible combinations of electron-helicity (Left or Right) and polarimeter-scattering-state (Up or Down), and computed the yields in these spectra. In obvious notation, the cross ratio r is defined to be the ratio of two geometric means, and is related to the asymmetry ξ,

$$r = \sqrt{\frac{N_{RU} N_{LD}}{N_{RD} N_{LU}}}, \qquad \xi = \frac{r-1}{r+1}. \tag{11}$$

In the cross-ratio method of analysis of the scattering asymmetries measured in the polarimeter, Ohlsen and Keaton (1973) showed that false asymmetries cancel to all orders from helicity-dependent errors in charge integration or system dead-times, or from errors in detection efficiency and acceptances; and that false asymmetries cancel to first order from misalignments with respect to $\vec{q}$, or from a difference in the beam polarization for the two helicity states.

4.5 Systematic Uncertainties

The systematic and scale uncertainties achieved in E93-038 are listed in Table 2, which is Table VIII of our archival Physical Review paper [Plaster et al. (2006)]. A significant merit of

Source	$\langle Q^2 \rangle$ [(GeV/c)^2]				
	$0.447^{(a)}$	$1.132^{(a)}$	$1.132^{(b)}$	$1.450^{(a)}$	$1.45^{(b)}$
Beam Polarization	1.6	0.7	0.4	1.2	0.3
Charge-Exchange	<0.1	<0.1	0.1	<0.01	0.2
Depolarization	<0.1	0.1	<0.1	<0.1	0.6
Positioning/Traceback	0.2	0.3	0.3	0.4	0.4
Precession Angle	1.1	0.3	0.1	0.5	0.1
Radiative Corrections	0.7	0.1	0.1	0.1	0.1
Timing Calibration	2.0	2.0	2.0	2.0	2.0
Total of Above Sources	2.9	2.2	2.1	2.4	2.2

(a) $\chi = \pm 40^\circ$ precession.
(b) $\chi = 0^\circ, \pm 90^\circ$ precession.

Table 2: Systematic and scale uncertainties in G_E^n/G_M^n [%] achieved in E93-038 (table from [Plaster et al. (2006)]).

our technique is that the systematic uncertainties are quite small, because both the beam polarization and polarimeter analyzing power cancel in the P_t/P_ℓ ratio. In E93-038, our results at all of our Q^2 points were statistics dominated, with the total (quadrature summed) systematic uncertainties on the order of $\sim 2.5\%$ [Plaster (2006)]. A few of the larger systematic uncertainties resulted from fluctuations in the beam polarization (between measurements of the asymmetries at different neutron spin precession angles χ), uncertainties in the spin precession angle χ (resulting from small differences between the measured field maps and those computed with finite-element-analysis codes), and a small dependence of the analysis results on the choice of the subset of data employed for the timing calibration of the polarimeter.

We project that the systematic uncertainties for our proposed measurements will, again, be quite small. The run plan will include ∼daily changes in the spin precession angle, frequent measurements of the beam polarization, and dedicated runs with a liquid hydrogen target to assess the level of contamination from (and also the asymmetry from) charge-exchange (p, n) reactions in the lead curtain at the polarimeter shielding hut entrance. We will also carry out detailed field maps of the dipole field to assess the uncertainty in the precession angle.

Finally, we emphasize that corrections for nuclear physics effects such as FSI, MEC, and IC are relatively small near the quasielastic peak, and will be applied in the same manner using the Arenhövel formalism as was employed for the analysis of the E93-038 data. The Arenhövel calculations for quasielastic scattering off of the deuteron have been thoroughly benchmarked in a number of different experiments probing various polarized and unpolarized $d(e, e'N)$ observables (e.g., [Boeglin (2008), Hu (2006)]).

4.6 Count Rates

The rate of electron-neutron coincidence events, which comes from quasielastic scattering of electrons on the 40-cm LD_2 target, was projected at $Q^2 = 4.0$, 5.2, and 6.9 (GeV/c)^2 for a beam current of 80 μA (which corresponds to a beam luminosity $L = 1.02 \times 10^{39}$ cm^{-2}s^{-1}). The calculation was done for a momentum bite $\Delta p/p$ of $-3/+15\%$ for the scattered electron. This SHMS momentum bite (combined with the cuts on the missing momentum and SHMS-NPOL coincidence time) helps to suppress the neutrons associated with pion production (see Figs. 19,

26 and Appendix A).

Four-Momentum Transfer, Q^2 (GeV/c)^2	4.0	5.2	6.9
SHMS Angular Acceptance:			
$\Delta\theta_e$ (mrad)	± 24	± 24	± 24
$\Delta\phi_e$ (mrad)	± 55	± 55	± 55
SHMS Efficiency, ϵ_e (%)	92	92	92
SHMS Momentum Bite, $\Delta p_e/p_e$ (%)	-3/+15	-3/+15	-3/+15
Neutron Polarimeter Angular Acceptance:			
$\Delta\theta_n$ (mrad)	± 60.0	± 60.0	± 60.0
$\Delta\phi_n$ (mrad)	± 99.7	± 99.7	± 99.7
Neutron Polarimeter Efficiency, ϵ_n (%)	4.0	5.0	5.9
Beam Current, I_{beam} (μA)	80	80	80
MCEEP Rate, $< R_{MCEEP} >$ (Hz)	73.0	52.7	39.1
Real-Event Rate, R_{real} (Hz)	2.93	2.64	2.29
Neutron Polarimeter Analyzing Power, A_Y	7.2	5.8	4.6
Precession Angle, χ (deg)	147.3	144.8	143.1
Expected Asymmetries:			
for -χ Precession (%)	-3.01	-2.14	-1.30
for +χ Precession (%)	1.29	0.96	0.61

Table 3: The neutron polarimeter and SHMS acceptances, estimated neutron polarimeter parameters, and calculated real event rate at Q^2 = 4.0, 5.2, and 6.9 (GeV/c)^2 for a beam current of 80 μA incident on a 40-cm LD_2 target in JLab Hall C. Also listed are the simulated NPOL efficiency and estimated analyzing power, and expected asymmetries for -χ and +χ precession of the neutron polarization vector.

We used the kinematic conditions from Table 1 for Q^2 = 4.0, 5.2, and 6.9 (GeV/c)^2. Based on the acceptance-averaged SHMS-NPOL coincidence rate of quasielastic events, $< R_{MCEEP} >$, from MCEEP [Ulmer (1991) version 3.9 includes radiative corrections], we estimated the real-event rate R_{real} for an assumed SHMS efficiency ϵ_{HMS} = 0.92, the SHMS momentum bite of -3/+15%, and the SHMS-NPOL coincidence time-of-flight ($cTOF$) window of ±1 ns. For this estimation, we simulated the neutron polarimeter efficiency, ϵ_n, (including loss of events due to analysis cuts) with the FLUKA 2008.3b.2 code (see also Section 5). To estimate the NPOL analyzing power, A_Y, we used the analyzing power A_Y = 14.4±1.3% measured in E93-038 at neutron momentum P_n = 1.45 MeV/c (see Plaster et al. (2006)) as well as an assumption that the analyzing power for the neutron scales the same way as the analyzing power for protons (see Azhgirei et al.(2005) and Fig. 20):

$$A_Y \sim 1 \,/\, P_{nucleon} \qquad or \qquad A_Y \cdot P_{nucleon} \;=\; const \tag{12}$$

Listed in Table 3 are neutron polarimeter and SHMS acceptances, estimated neutron polarimeter parameters (viz., A_Y and ϵ_n), and the calculated real event rates in Hall C.

4.7 Projected Uncertainties

To estimate statistical uncertainties, we use the simple pairwise analysis here, but the actual analysis in the experiment will include acceptance averaging using methods similar to E93-038.

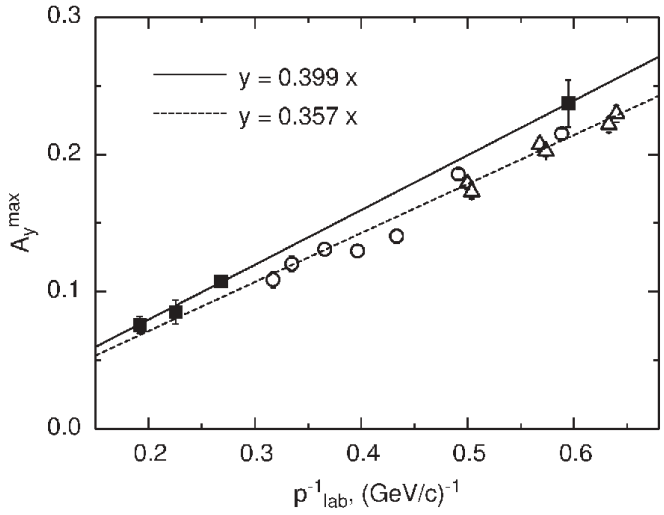

Figure 20: Momentum dependence of an analyzing power measured for protons on CH_2 and C (Azhgirei et al.(2005)). Solid line – fit of CH_2-data, dashed line – fit of C-data.

The up-down asymmetry, measured in JLab E93-038, is proportional to the projection of the neutron polarization vector on the axis that is perpendicular to the neutron momentum direction. Thus, the ratio of asymmetries for neutron spin precession through $\pm\chi$ degrees is given by:

$$\eta \equiv \frac{\xi_-}{\xi_+} = \frac{P_-^x}{P_+^x} = \frac{P_{S'}cos(-\chi) + P_{L'}sin(-\chi)}{P_{S'}\ cos(\chi) + P_{L'}\ sin(\chi)} = \frac{(P_{S'}/P_{L'})\ cos(\chi) - sin(\chi)}{(P_{S'}/P_{L'})\ cos(\chi) + sin(\chi)} \tag{13}$$

$$(P_{S'}/P_{L'}) = \frac{-sin(\chi)\ (\eta+1)}{cos(\chi)\ (\eta-1)} = -tan(\chi)\ \frac{(\eta+1)}{(\eta-1)} \tag{14}$$

where $P_{S'}$ and $P_{L'}$ are transverse and longitudinal projections of the neutron polarization vector:

$$P_{S'} = -h\ P_e\ \frac{K_S\ g}{K_0\ (1\ +\ g^2/K_0)} \tag{15}$$

$$P_{L'} = h\ P_e\ \frac{K_L}{K_0\ (1\ +\ g^2/K_0)} \tag{16}$$

Here h is the beam helicity, P_e is the beam polarization, and $g \equiv (G_E/G_M)$.

$$(P_{S'}/P_{L'}) = -g\ (K_S/K_L) \tag{17}$$

From (17) and (14) :

$$g = -\left(\frac{K_L}{K_S}\right)\ \left(\frac{P_{S'}}{P_{L'}}\right) = \left(\frac{K_L}{K_S}\right)\ tan(\chi)\ \frac{(\eta+1)}{(\eta-1)} \tag{18}$$

The statistical uncertainty in the g value is:

$$(\delta g)_{stat} = \left(\frac{K_L}{K_S}\right)\ tan(\chi)\ \frac{2}{(\eta-1)^2}\ \delta\eta \tag{19}$$

The relative statistical uncertainty $(\delta g/g)_{stat}$ is:

$$\left(\frac{\delta g}{g}\right)_{stat} = \frac{2}{(\eta+1)(\eta-1)}\ \delta\eta \tag{20}$$

Here $\delta\eta$ is the statistical error in the asymmetry ratio:

$$\left(\frac{\delta\eta}{\eta}\right)^2 \;=\; \left(\frac{\delta\xi_-}{\xi_-}\right)^2 \;+\; \left(\frac{\delta\xi_+}{\xi_+}\right)^2 \tag{21}$$

or

$$(\delta\eta)^2 \;=\; \left(\frac{\delta\xi_-}{\xi_+}\right)^2 \;+\; \xi_-^2\left(\frac{\delta\xi_+}{\xi_+^2}\right)^2 \tag{22}$$

To project the statistical uncertainties, we used the statistical errors for asymmetries which come from Poisson statistics:

$$\left(\frac{\delta\xi_\pm}{\xi_\pm}\right)^2 \;=\; \frac{1}{\xi_\pm^2}\left(\frac{1+2/r}{N_\pm}\right) \;=\; \frac{1}{(A_Y P_\pm^x)^2}\left(\frac{1+2/r}{N_\pm}\right) \tag{23}$$

Here $N_\pm$ is the number of events taken during $\pm\chi$ precession angle runs, A_Y is the polarimeter analyzing power, and r is the ratio of real-to-accidental coincidences. For these projections, we used the value r = 22.5, 13.2, and 6.4 from the simulation for an 80 μA beam at Q^2 = 4.0, 5.2, and 6.9 (GeV/c)^2, respectively. To estimate accidental coincidence rates ($\sim$0.13, 0.20, and 0.36 Hz), the electron single rates in the SHMS ($\sim$0.52, 0.41, and 0.47 kHz) were calculated with the MONQEE code (Dytman 1987). The rates of accepted events in the polarimeter from inclusive neutrons ($\sim$126, 240, 387 kHz) were estimated via the flux of inclusive neutrons simulated with the program of P. Degtyarenko (see Figs. 21, 22, 23) that was convoluted with the polarimeter efficiency to low- and medium-energy neutrons that was simulated with FLUKA2008.3b.2 program on the same manner as for quasielastic neutrons. Degtyarenko's program, based on GEANT 3.21 (Brun 1993), uses the GCALOR (Zeitnitz 1994) program package in order to simulate hadronic interactions down to 1 MeV for nucleons and charged pions and into the thermal region for neutrons, and uses DINREG (Degtyarenko 1992, 2000) – Deep Inelastic Nuclear Reaction Exclusive Generator with a model for hadronic interactions of electrons and photons. Values of r achieved in E93-038 are compared with the results of the simulation in Fig. 30.

The projected uncertainties ΔG_E^n are plotted in Fig. 24 as a function of the data acquisition time for a luminosity of 1.02×10^{39} cm^{-2}s^{-1}, which is achievable with a beam current of 80 μA on a 40-cm liquid deuterium target. The DAQ time that is designated by the dotted line in Fig. 24 was chosen to target an uncertainty $[\Delta G_E^n]$ in the vicinity of 0.0010.

Figure 25 shows the statistical uncertainties $\Delta g/g$, projected at Q^2 = 4.0, 5.2, and 6.9 (GeV/c)^2 for the DAQ time of 240, 260, and 720 hours (respectively) as a function of precession angle χ.

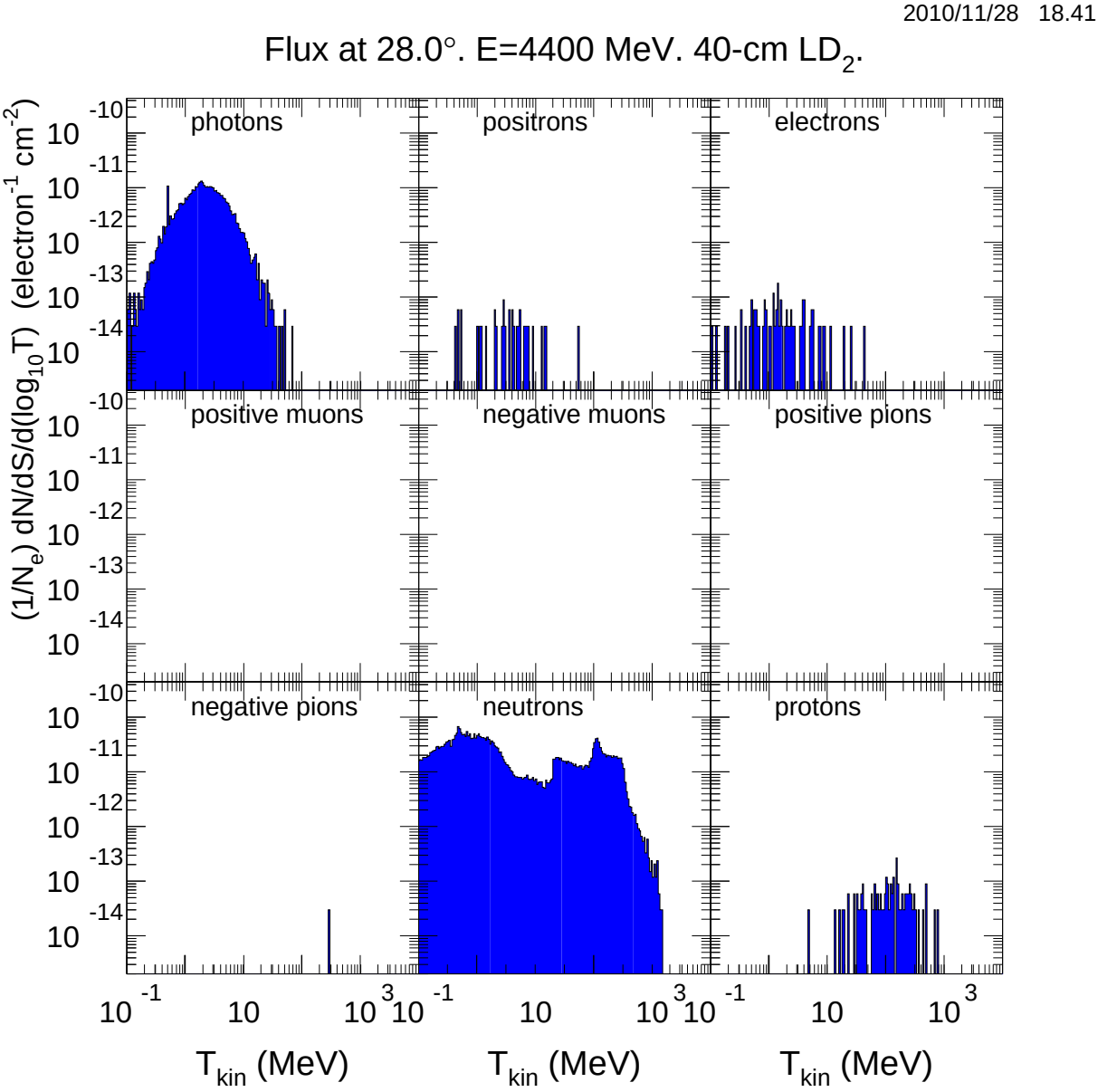

Figure 21: Simulated spectra of the particles at 28^o from 4.4 GeV electron beam incident on a 40-cm LD_2 target.

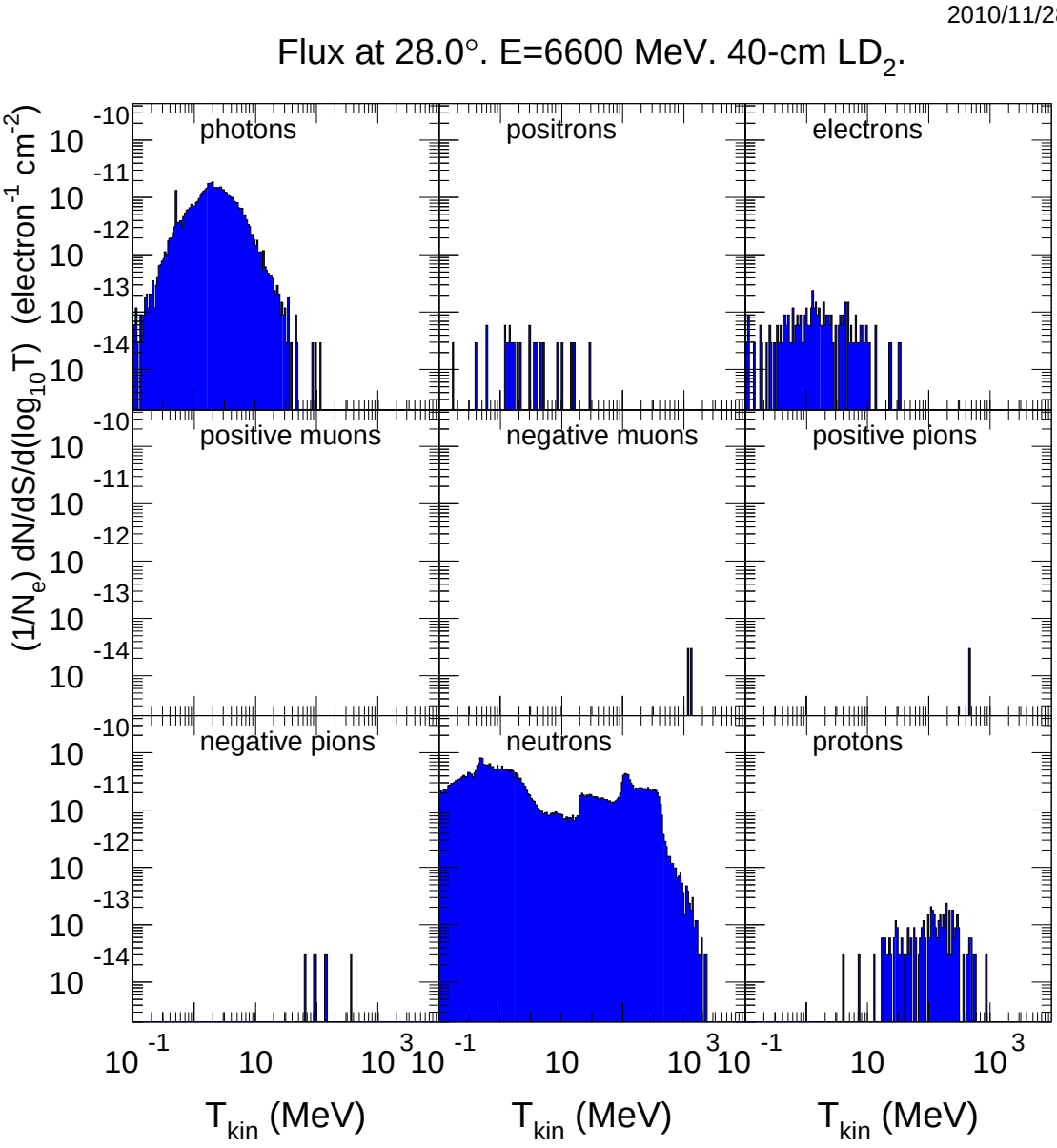

Figure 22: Simulated spectra of the particles at 28^o from 6.6 GeV electron beam incident on a 40-cm LD_2 target.

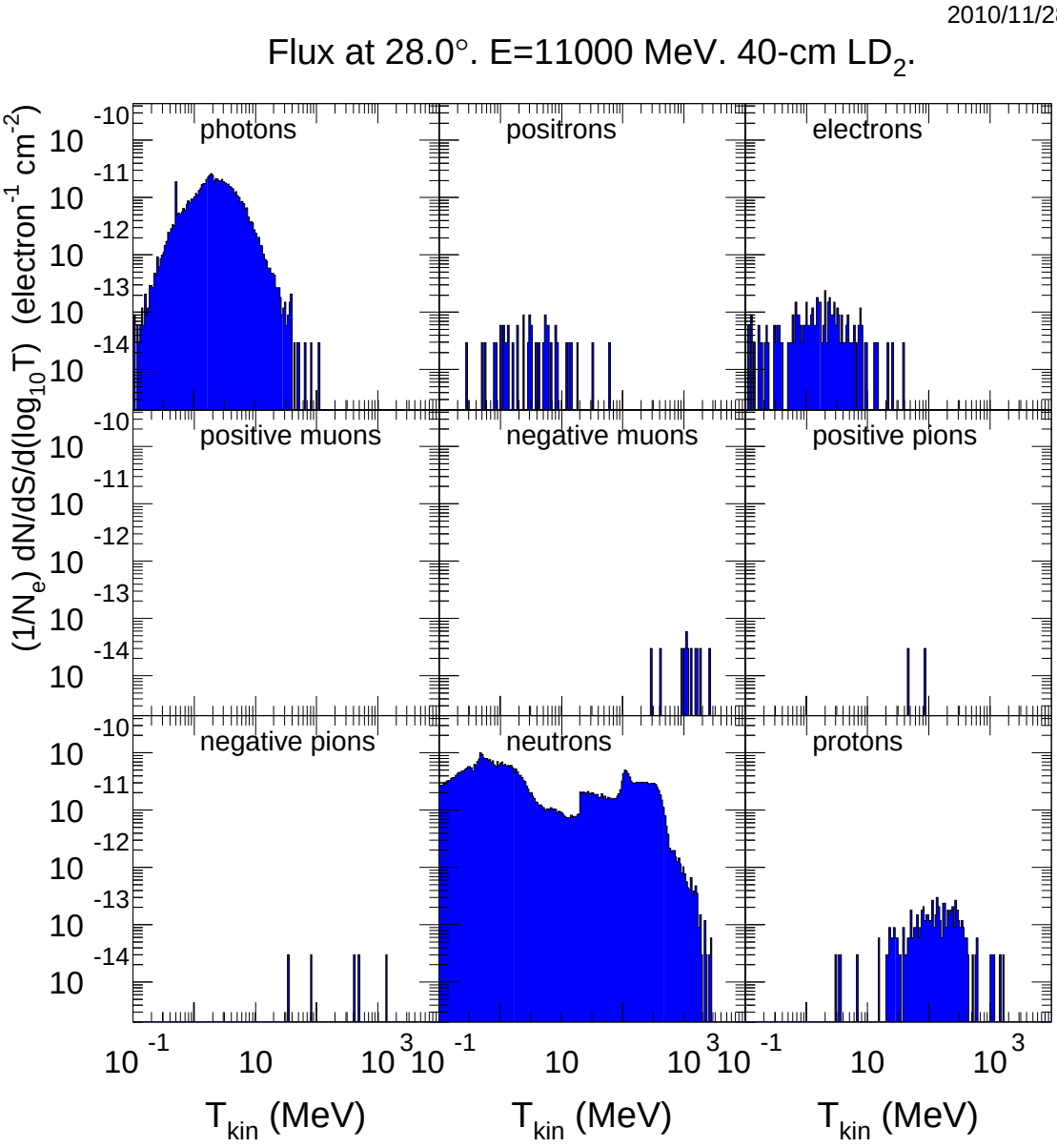

Figure 23: Simulated spectra of the particles at 28^o from 11.0 GeV electron beam incident on a 40-cm LD_2 target.

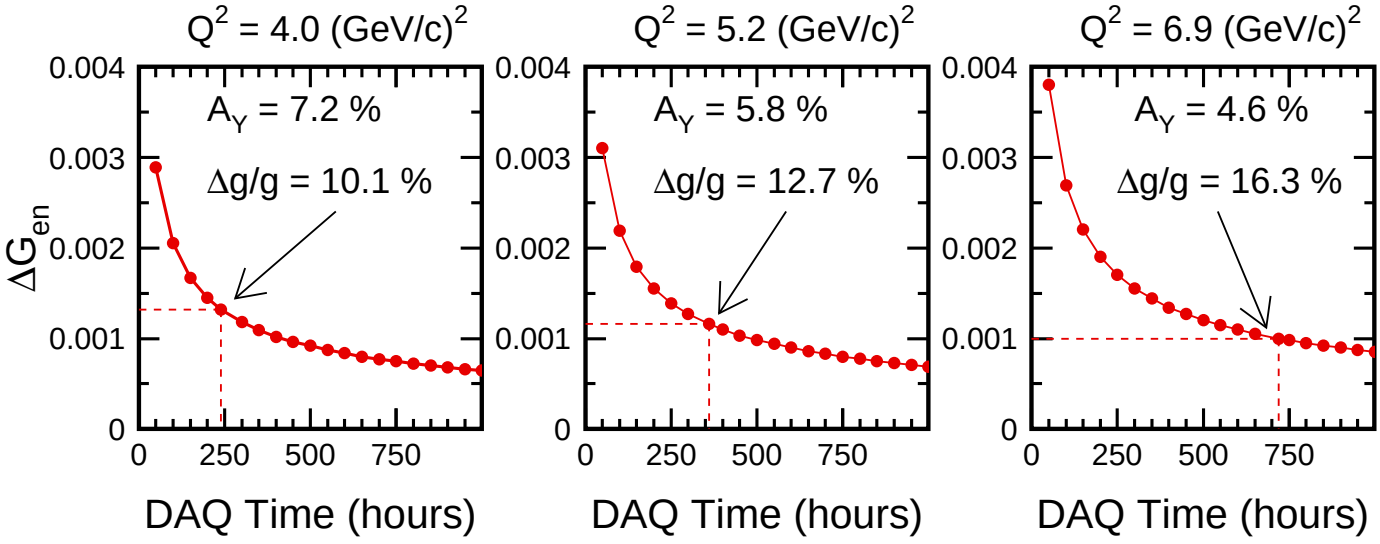

Figure 24: Projected uncertainties ΔG_E^n at $Q^2 = 4.0$, 5.2, and 6.9 $(\mathrm{GeV/c})^2$ for a beam current of 80 μA as a function of the DAQ time in Hall C. BLAST fit parameterization for G_E^n is assumed.

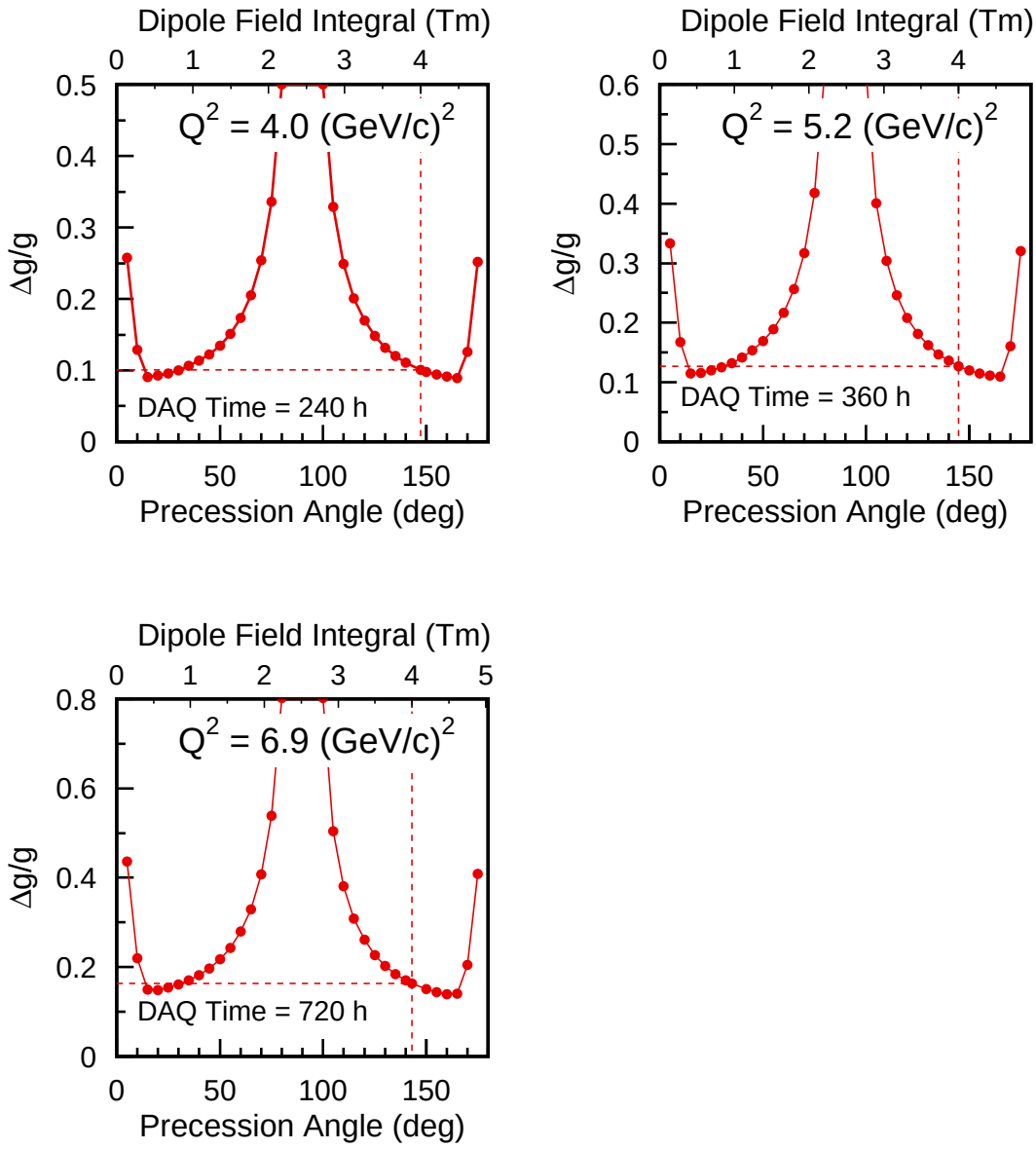

Figure 25: Statistical uncertainties $\Delta g/g$, projected at $Q^2 = 4.0$, 5.2, and 4.3 $(\mathrm{GeV/c})^2$, as a function of precession angle χ.

5 Some Results from E93-038

The purpose of this section is to indicate the quality of the data obtained and the simulation made in E93-038. We selected real quasielastic $^2H(\vec{e}, e'\vec{n})$ events using a restricted HMS momentum bite, the cut on the missing momentum, and a cut on HMS-NPOL coincidence time (see Fig. 26).

Typical time-of-flight spectra for the highest Q^2 [viz., $Q^2 = 1.45$ $(\mathrm{GeV/c})^2$] are shown in Fig. 27. The left panel is an HMS-NPOL coincidence time-of-flight spectrum. We compared the measured time-of-flight, cTOF, with the time-of-flight calculated from electron kinematics and offsets determined by a calibration procedure; the result is centered on zero with a FWHM of approximately 1.5 ns, and the reals-to-accidentals ratio is ≈ 12 at a beam current of ≈ 50 μA [see Fig. 30]. The right panel is the time-of-flight spectrum between a neutron event in the front array

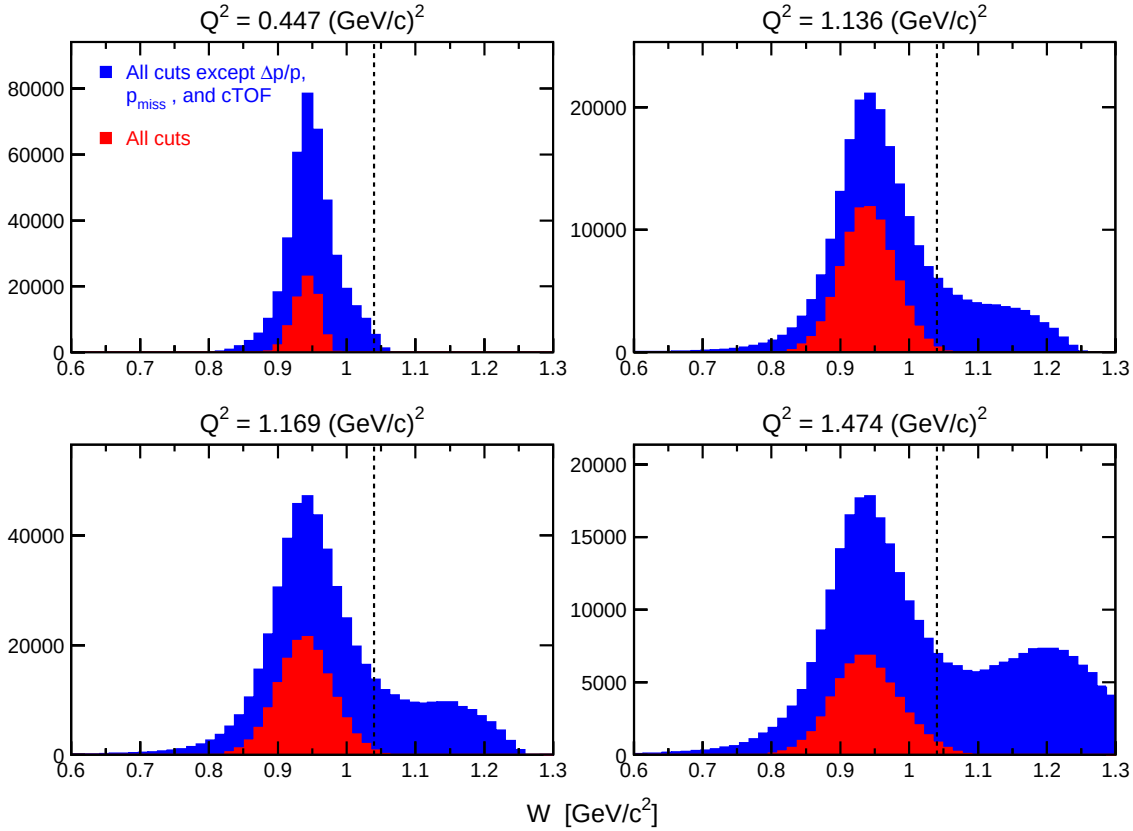

Figure 26: Invariant mass spectra before and after cuts on the scattered electron momentum, the missing momentum, and an HMS-NPOL coincidence time-of-flight.

and an event in the top or bottom rear array. We compared this measured time-of-flight, ΔTOF, with the time-of-flight calculated for elastic np scattering. This result, normalized to the nominal 2.5 m flight path, has a peak at zero also. The tail on the slow side is due to scattering from carbon, and the secondary peak at ~ -2.5 ns is the result of π^0 production in the front array. To extract the physical scattering asymmetry, we calculated the cross ratio, r, which is defined to be the ratio of two geometric means, $(N_U^+ N_D^-)^{1/2}$ and $(N_U^- N_D^+)^{1/2}$, where $N_U^+(N_D^-)$ is the yield in the ΔTOF peak for neutrons scattered up(down) when the beam helicity was positive(negative); the yields, corrected for background, were obtained by peak fitting. The physical scattering asymmetry is then given by $(r-1)/(r+1)$. The merit of the cross ratio technique [Ohlsen (1973)] is that the neutron polarimeter results are independent of the luminosities for positive and negative helicities, and the efficiencies and acceptances of the top and bottom halves of the polarimeter. Beam charge asymmetries (of typically 0.1%) and detector threshold differences cancel in the cross ratio.

The result of an analysis of the asymmetries for each run at $Q^2 = 1.13$ (GeV/c)^2 and the error-bar weighted average for these data appear in Fig. 28; the sign of the asymmetries from runs with the $\lambda/2$-plate IN have been reversed. A histogram of the asymmetries (see Fig. 29) clearly demonstrates that the distribution of the asymmetries is of an appropriate Gaussian shape.

To estimate the reals-to-accidentals ratio r, we simulated the rate of inclusive electrons in the HMS with the MONQUEE code [Dytman (1987)], and we used single rates in NPOL simulated with the GEANT-based program of P. Degtyarenko (for details, see Section 4.7). Simulated accidental coincidence rates and r-values are shown in Fig. 30 together with ones measured in E93-038. The difference between the measured and calculated accidentals and the ratios of real-

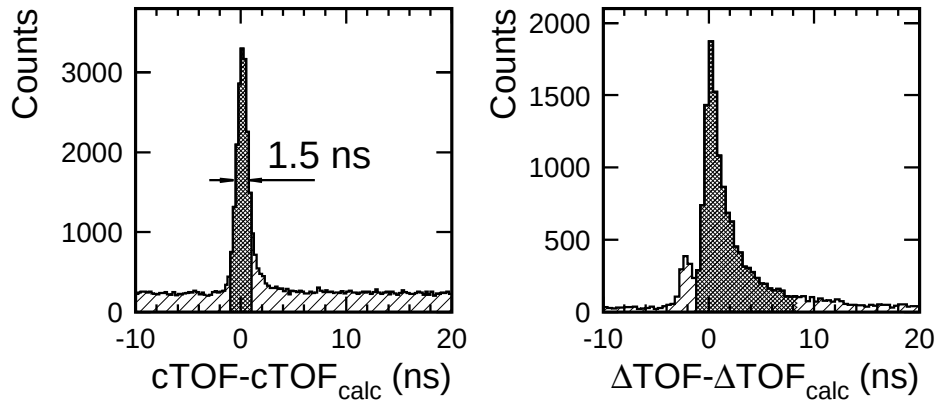

Figure 27: Typical time-of-flight spectra for $Q^2 = 1.45$ (GeV/c)^2. Selected portions are shaded.

to-accidental coincidences at $Q^2 = 0.45$ (GeV/c)^2 is because the calculation doesn't take into account the larger radiation background in Hall C caused by multiple scattering of electrons at this lowest beam energy of 884 MeV.

We simulated the E93-038 neutron polarimeter efficiency, ϵ_n, (including the neutron transmission through the 10-cm lead curtain) using the FLUKA-2002 program, version 2.0 [Fasso et al. (2001)]. The "stand-alone" (not GEANT-based) FLUKA-2002 code is a general purpose Monte Carlo code for studying transport and interactions of particles in a material over a wide energy range. The program is best known for its hadron event generators; the used version of the code can also handle (with similar or better accuracy) muons, low-energy neutrons, and electromagnetic effects. Figure 31 (left panel) indicates good agreement of the results of the simulation with NPOL efficiencies extracted from the E93-038 data [Semenova et al. (2003)]. Both simulation and data analysis were made for the front (rear) array threshold of 8 (20) MeVee. Simulating the analyzing power (A_Y) for the E93-038 polarimeter, for elastic *n-p* and quasielastic scattering events in the front array, we determined (*in the rest frame of the target nucleon*) A_Y values from the partial-wave analysis embodied in the Scattering Analysis Interactive Dial-In (SAID) code [Arndt (1977, 2000)]. In our simplified approach, we supposed that $A_Y = 0$ for both inelastic reactions and multiple scattering events. Probably, this assumption leads to the disagreement between the simulated (and averaged over the NPOL acceptance) and the measured analyzing power at the low neutron energy of 239 MeV. Nevertheless, at higher neutron energies ($T_n = 608$ and 786 MeV), *the simulated and measured in E93-038 A_Y values are in very good agreement* (see right panel in Fig. 31).

The beam polarization measured in March 2001 is plotted in Fig. 32. The mean polarization during this two-weeks period was 82.2±0.1 (-81.0±0.2)% with the $\lambda/2$ wave plate "OUT" ("IN").

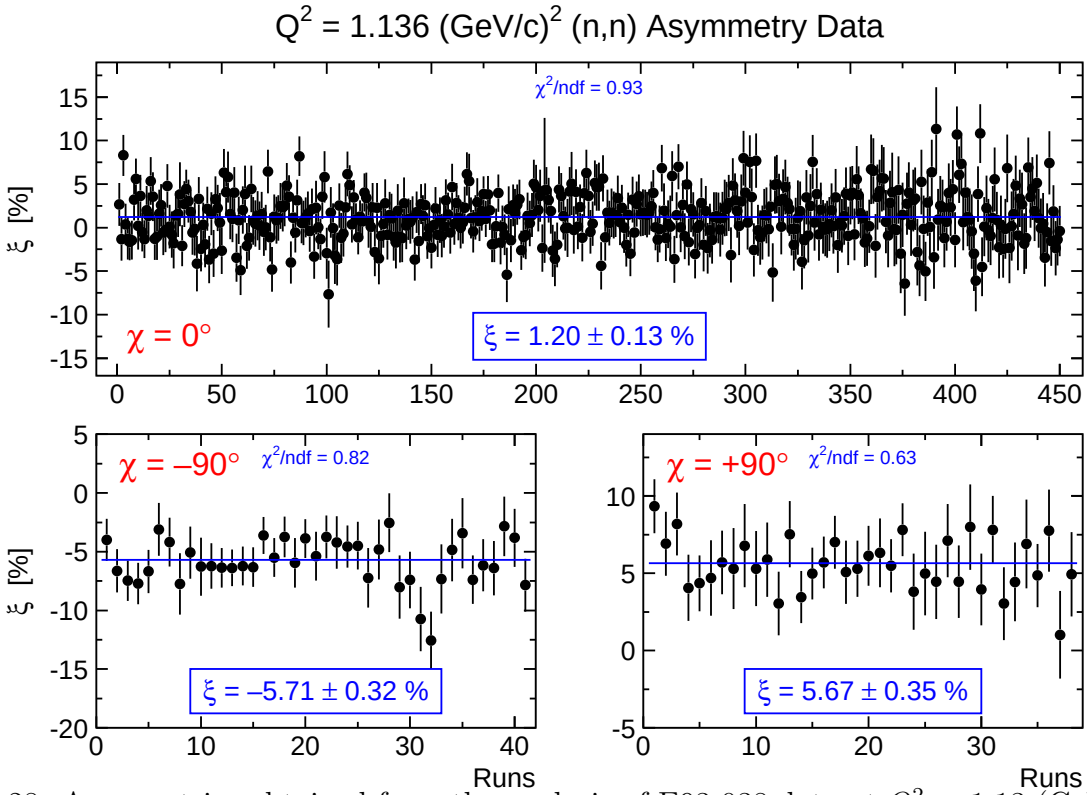

Figure 28: Asymmetries obtained from the analysis of E93-038 data at $Q^2 = 1.13$ (GeV/c)^2.

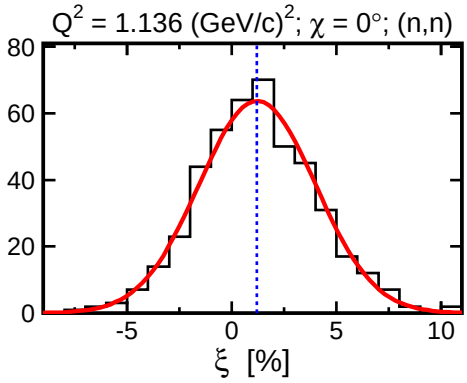

Figure 29: Histogram of E93-038 asymmetries at $Q^2 = 1.13$ (GeV/c)^2 ($\chi = 0^o$). The solid curve is a Gaussian fit, and the vertical dashed line is the mean value of the asymmetry from Fig. 28.

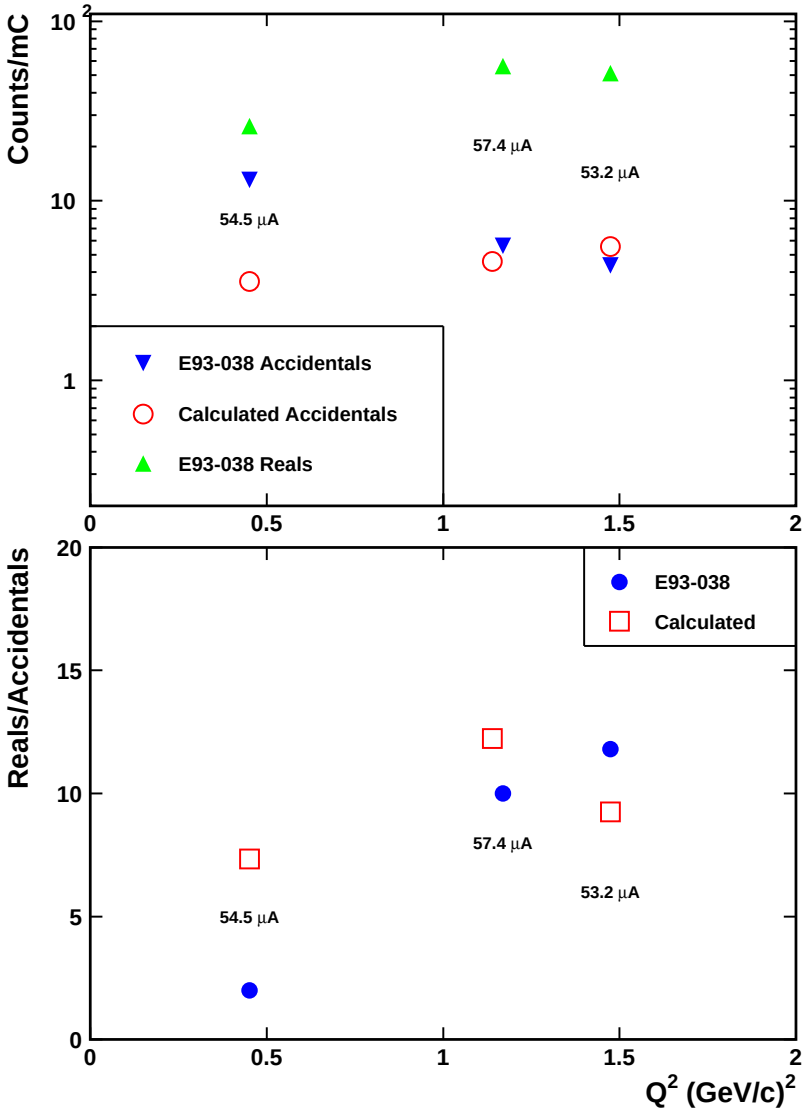

Figure 30: Real event rate, accidental coincidence rate, and the reals-to-accidentals ratio obtained from E93-038. The target-front array flight path was 7 m for NPOL at 46 degrees.

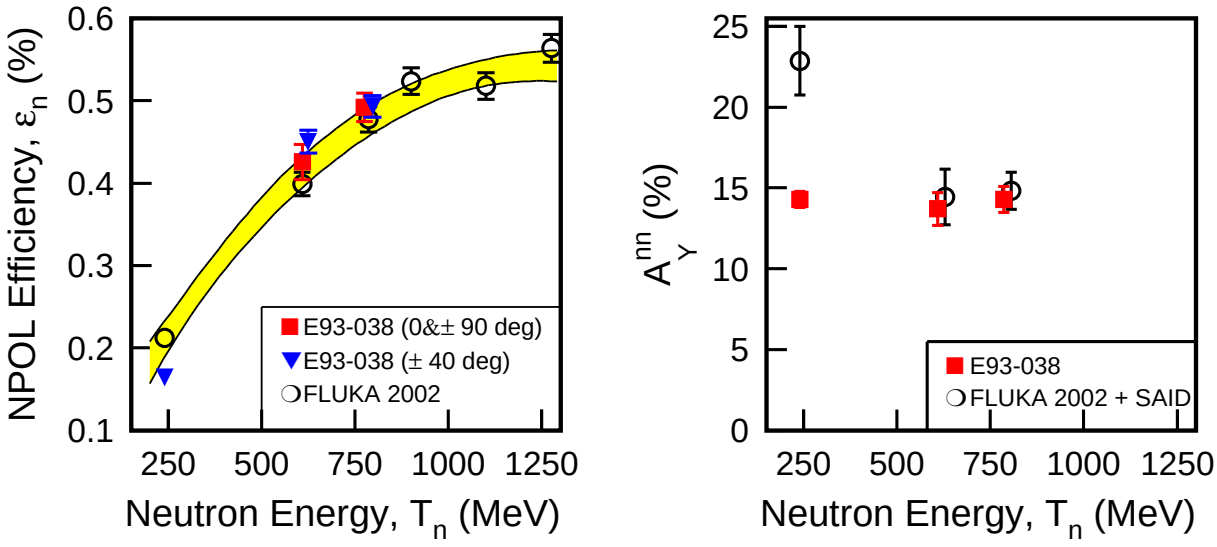

Figure 31: Comparison of the simulated neutron polarimeter parameters (viz., analyzing power, A_Y, and the neutron polarimeter efficiency, ϵ_n) with the results from E93-038. The shaded band in the left panel shows an uncertainty on the fit of the simulated efficiencies with a polynomial function.

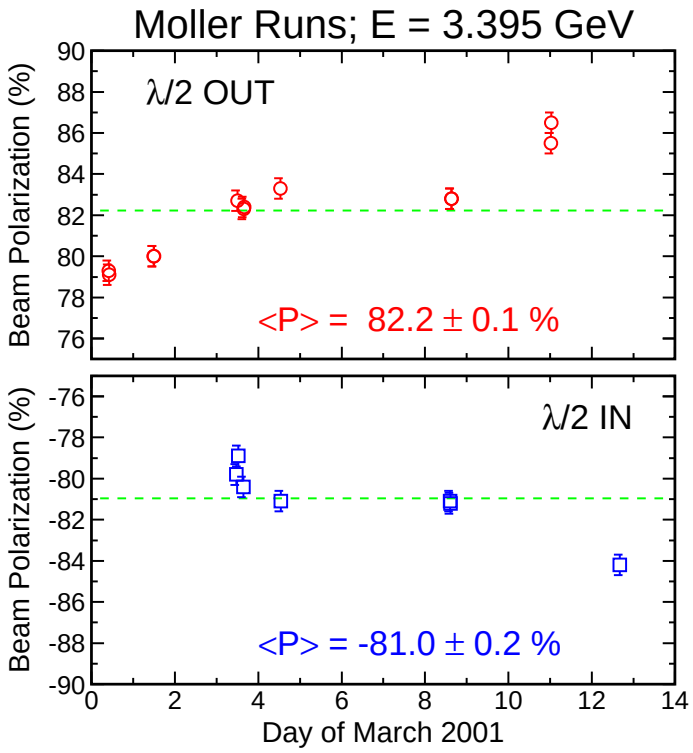

Figure 32: Electron beam polarization in March 2001.

6 Beam Time

Our beam-time request for measuring G_E^n at $Q^2 = 4.0$, 5.2, and 6.9 (GeV/c)^2 is shown in Table 4. We estimate that a total data acquisition time of 60 days in Hall C will be needed to produce a statistical uncertainty ΔG_E^n in the vicinity of 0.001 at each of the Q^2 points. The estimated acquisition times for runs on a 15-cm LH_2 target will be needed to assess the false asymmetry or dilution from the two-step process d($\vec{e}$,e'$\vec{p}$)n + Pb($\vec{p}$,$\vec{n}$).

G_E^n physics measurements Q^2 [(GeV/c)^2]	4.0	5.2	6.9	Total
LD_2 target	10	15	30	55
LH_2 target	0.5	0.5	0.5	1.5
Dummy target	0.1	0.1	0.2	0.5
Beam polarization	0.3	0.5	1	2
Time calibrations [LD_2 target]	0.1	0.1	0.2	0.5
Overhead	0.1	0.1	0.3$^{(a)}$	0.5
Total physics measurements	11.1	16.5	32.4	60

Table 4: Beam-time [days] for measuring G_E^n at $Q^2 = 4.0$, 5.2, and 6.9 (GeV/c)^2 for an 80 μA, 80% polarized beam on a 40-cm LD_2 target.

(a) 40 changes in dipole current, 9 target changes, starting and stopping the DAQ system for runs that are typically 5 hours long.

Also needed will be seven days of commissioning time with beam to check out the spectrometer, the Moeller polarimeter, and the neutron polarimeter [NPOL] and electronics. NPOL checkout includes checking all detectors and detector thresholds, adjusting timing, adjusting the thickness of the Pb curtain and determining the optimal beam current, and checking room background with a shadow shield. Seven days will be required without beam for pulse-height calibrations and cosmic ray tests of the polarimeter detectors.

7 Collaboration

Most of the participants listed earlier contributed to the success of E93-038. The collaboration is a strong, experienced, and large team (currently about 80 scientists from 30 institutions). Graduate students and postdocs will be added after the proposed experiment is approved and scheduled. As in E93-038, Kent State University (KSU) will be responsible for the neutron polarimeter; MIT, for the neutron spin-precession dipole magnet; and JLab for the magnetic spectrometer [SHMS]. KSU provided the neutron detectors in the top/bottom arrays and the polarimeter electronics; Hampton University provided ten of the neutron detectors in the analyzer array, while JLab provided another ten. The University of Virginia provided the tagger detectors used in E93-038. Duke University took responsibility for the Analysis Engine and also for setting up the electronics and timing. Professor Bradley Plaster at the University of Kentucky will be responsible for modification of analysis programs and upgrading the simulation programs used in E93-038. Plaster is the lead author on the archival paper on E93-038 [Phys.Rev.C73, 025205 (2006)]. Dr. A.Yu. Semenov (University of Regina) functioned as the coordinator of the E93-038 analysis effort. T. Reichelt (Bonn), H. Fenker (JLab), and S. Danagoulian (NCAT) were

the lead scientists in establishing the operating conditions for running the Moeller polarimeter at a beam energy below one GeV, and in setting up and running the Moeller polarimeter at the two higher energies. Professor Stanley Kowalski has reaffirmed his commitment to oversee that the Bates engineering lab will modify dipole magnet and he will be responsible for the field mapping.

8 Equipment Needs for Neutron Polarimeter

The equipment needs are shown in Table 5. A number of the 10 cm×10 cm×100 cm detectors needed for the polarimeter already exist at JLab, and several more will be obtained by cutting and machining existing larger detectors at Kent State and Northern Michigan Universities. Some of the needed 1 cm×10 cm×106 cm veto detectors may also exist, but the total needed are budgeted here. As indicated, some of the needed 2 inch diameter fast phototubes also exist, but the majority will need to be purchased. Kent State will provide custom designed fast amplifiers for the anode signals and Hall C will provide all other electronics.

New electronics needs for the enhanced polarimeter include constant fraction discriminators, 400 ns delay lines, an additional control box, and additional PMT bases and preamps. We are requesting JLab to provide the delay lines; KSU would provide the preamps, the control box, and the PMT bases. Constant fraction discriminators will be used on all the mean-timed scatterer detectors and the necessary units to do this are available from existing quad CF units owned by Kent State and units that can be borrowed from Tel Aviv U. and Michigan State U. Flash ADC's available from Hall C will be used for timing on the top and bottom E-detectors.

Equipment items that need to be purchased are summarized in Table 5. Funds will be sought from DOE and NSF by the participating institutions. B. Plaster at the University of Kentucky has made a commitment to seek funds for the front veto detectors, and M. Elaasar (Southern University at New Orleans) has made a commitment to seek funds for the rear veto detectors. The University of Regina and Argonne National Lab. groups may seek funds also because there may not be enough from the other two or one or both may not succeed.

The experiment needs a dipole for precession of the neutron spin and to sweep away charged particles. We plan to use the BM-111 dipole, previously used at the Argonne ZGS (Zero Gradient Synchrotron). The magnet is no longer in use at Argonne, and is available for us to use for this proposal. The initial information provided was that the effective length of the dipole is 2 m with a 2-2.2 T maximum field for a field integral of ≈4 Tm. The gap is nearly 20 cm, and the width approximately 1 m. We are getting full specifications of the dipole, but the magnet appears sufficient. We will reconfigure the dipole to have tapered poles, to maintain a field integral of ≈4 Tm, while maximizing the acceptance. We can live with slightly below 4 Tm, if this is necessary to get the full acceptance, but we will optimize the field integral vs. acceptance once we have the complete specifications for the magnet. The magnet's power supply is also available, but it is not clear that it is in good enough condition that it makes sense to refurbish it, or if a new power supply will be necessary.

Table 5: NPOL equipment items to be purchased.

		Cost
1	**Scintillator Detectors**	
1.1	88 [10 cm×10 cm×100 cm] Scintillator & Light Pipes Have 40 (KSU, JLab, Hampton), Kent State will provide 20 by cutting and machining existing detectors, purchase 28 at $1500 each.	$42,000
1.2	51 [1 cm×10 cm×106 cm] Veto Scintillator & Light Pipes	$51,000
1.3	280 Photomultiplies Tubes 2-inch diameter fast PMTs for 139 mean-timed detectors with 2 spares. Have 80, need 200 at $1000 each.	$200,000
1.4	280 Magnetic Shields (for 2-in diam PMT)	$40,000
2.	**Electronic Modules**	
2.1	Fast amplifiers [Provided by Kent State]	0
2.2	Fast discriminators, ADCs, TDCs, Power Supplies, etc... [Provided by Hall C]	0
	Subtotal Detectors and Electronics	**$333,000**

References

[Alexandrou 2006] C. Alexandrou, G. Koutsou, J.W. Negele, and A. Tsapalis, Phys. Rev. **D74**, 034508 (2006).

[Arenhoevel 1987] H. Arenhoevel, Phys. Lett. **B199**, 13 (1987).

[Arenhoevel 1988] H. Arenhoevel *et al.*, Z. Phys. **A331**, 123 (1988).

[Arenhoevel 2002] H. Arenhoevel, private communication (2002).

[Arndt 1977] R.A. Arndt, R.H. Hackman, and L.D. Roper, Phys. Rev. **C15** 1002 (1977).

[Arnold 1981] R. G. Arnold, C. E. Carlson, and F. Gross, Phys. Rev. C **23**, 363 (1981).

[Arndt 2000] R. A. Arndt, L. D. Roper *et al.*, Scattering Analysis Interactive Dial-In (SAID) Program. Virginia Polytechnic Institute and State University, Unpublished. The Virginia Tech Partial-Wave Analysis Facility is still available from the original web site *http://said.phys.vt.edu/*. This facility is available on-line at *http://www.gwdac.phys.gwu.edu/* from the CNS Data Analysis Center at The George Washington University.

[Arrington 2007] J. Arrington and I. Sick, Phys. Rev. **C76**, 035201 (2007).

[Azhgirei 2005] L.S. Azhgirei et al., Nucl. Instrum. Meth. **A538**, 431 (2005).

[Aznaurian 1993] I.G. Aznaurian, Phys. Lett. **B316**, 391 (1993).

[Beck 1992] G. Beck and H. Arenhoevel, Few Body Systems **13**, 165 (1992).

[Bermuth 2003] J. Bermuth et al., Phys. Lett. **B564**, 199 (2003) updates D. Rohe *et al.*, Phys. Rev. Lett. **83**, 4257 (1999).

[Bijker 2004] R. Bijker and F. Iachello, nucl-th/0405026, accepted for publication in Phys. Rev. C (2004).

[Bodek 2008] A. Bodek et al., Eur. Phys. J. C **53**, 349 (2008).

[Boffi 2002] S. Boffi, L. Ya. Glozman, W. Klink, W. Plessas, M. Radici, and R. F. Wagenbrunn, Eur. Phys. J. A **14**, 17 (2002); W. Plessas, S. Boffi, L. Ya. Glozman, W. Klink, M. Radici, and R. F. Wagenbrunn, Nucl. Phys. A **699**, 312c (2002); R. F. Wagenbrunn, S. Boffi, W. Klink, W. Plessas, and M. Radici, Phys. Lett. B **511**, 33 (2001).

[Brun 1993] R. Brun et al. *GEANT Detector Description and Simulation Tool.* CERN Program Library Long Writeup W5013, September, 1993.

[Cardarelli 2000] F. Cardarelli, S. Simula, Phys. Rev. **C62**, 065201 (2000); S. Simula (private communication).

[Cecil 1979] R. Cecil, B.D. Anderson, R. Madey. Nucl. Instrum. Meth. **161**, 439 (1979).

[Chung 1991] P.L. Chung and F. Coester, Phys. Rev. **D44**, 229 (1991).

[Cloet 2008] I.C. Cloet et al., arXiv:nucl-th/0812.0416 (2008).

[Degtyarenko 1992] P.V. Degtyarenko, M.V. Kossov. *Monte Carlo Program for Nuclear Fragmentation*. Preprint ITEF 11-92, Moskow (1992).

[Degtyarenko 2000] P.V. Degtyarenko, M.V. Kossov, and H.-P. Wellisch. *Chiral invariant phase space event generator*. Eur. Phys. J. A **8**, 217-222 (2000); A **9**, 411-420 (2000); A **9**, 421-424 (2000).

[Dong 1998] S.J. Dong, K.F. Liu, and A.G. Williams, Phys. Rev. **D58**, 074504 (1998).

[Drechsel 1989] D. Drechsel and M.M. Giannini, Rep. Prog. Phys. **52**, 1083 (1989).

[Dytman 1987] S. Dytman, private communication (1987).

[Eden 1994] T. Eden *et al.*, Phys. Rev. **C50**, R1749 (1994).

[Edwards 2006] R.G. Edwards *et al.*, Phys. Lett. **96**, 052001 (2006).

[Fasso 2001] A. Fasso, A. Ferrari, P.R. Sala, Electron-Photon Transport in FLUKA: Status, Proceedings of the Monte Carlo 2000 Conference, Lisbon, October 23-26, 2000, A. Kling, F. Barao, M. Nakagawa, L. Tavora, P. Vaz eds., Springer-Verlag Berlin, pp. 159-164 (2001).

[Fasso 2001a] A. Fasso, A. Ferrari, J. Ranft, P.R. Sala, FLUKA: Status and Perspective for Hadronic Applications, Proceedings of the Monte Carlo 2000 Conference, Lisbon, October 23-26, 2000, A. Kling, F. Barao, M. Nakagawa, L. Tavora, P. Vaz eds., Springer-Verlag Berlin, pp. 955-960 (2001).

[Feshbach 1967] H. Feshbach and E. Lomon, Rev. Mod. Phys. **39**, 611 (1967).

[Frank 1996] M.R. Frank, B.K. Jennings, and G.A. Miller, Phys. Rev. **C54**, 920 (1996).

[Friar 1990] J.L. Friar, Phys. Rev. **C42**, 2310 (1990).

[Gari 1985] M.F. Gari and W. Krumpelmann, Z. Phys. **A322**, 689 (1985).

[Gari 1992] M.F. Gari and W. Krumpelmann, Phys. Lett. **B274**, 159 (1992).

[Galster 1971] S. Galster, H. Klein, J. Moritz, K.H. Schmidt, D. Wegener, and J. Bleckwenn, Nucl. Phys. **B32**, 221 (1971).

[Gayou 2002] O. Gayou *et al.*, Phys. Rev. Lett. **88**, 092301 (2002).

[Geis 2008] E. Geis *et al.*, Phys. Rev. Lett. **101**, 042501 (2008).

[Glazier 2005] D.I. Glazier *et al.*, Eur. Phys. J. **A24**, 101 (2005).

[Golack 2001] J. Golak, G. Ziemer, H. Kamada, H. Witala, and W. Glöckle, Phys. Rev. C **63**, 034006 (2001) applies FSI corrections to J. Becker *et al.*, Eur. Phys. J. A **6**, 329 (1999).

[Hagler 2007] Ph. Hagler *et al.*, arXiv:0705.4295 [hep-lat] (2007).

[Herberg 1999] C. Herberg *et al.*, Eur. Phys. J. **A5**, 131 (1999) applies FSI corrections to M. Ostrick *et al.*, Phys. Rev. Lett. **83**, 276 (1999).

[Holzwarth 2002] G. Holzwarth, hep-ph/020138; Z. Phys. **A356**, 339 (1996).

[Iachello 1973] F. Iachello, A.D. Jackson, and A. Lande, Phys. Lett. **43B**, 191 (1973).

[Iachello 2003] F. Iachello, Proceedings of 4th Int. Conference on Perspectives in Hadronic Physics, Trieste, Italy (2003). To be published in Eur. Phys. J.

[Isgur 1998] N. Isgur, Phys. Rev. Lett. **83**, 272 (1999).

[Isgur 2000] N. Isgur and J.W. Negele, Nuclear Theory with Lattice QCD, a proposal to DOE, PI's (2000).

[Ji 1991] X. Ji, Phys. Lett. **B254**, 456 (1991).

[Jones 2000] M. Jones *et al.*, Phys. Rev. Lett. **84**, 1398 (2000).

[Kaskulov (2003)] M.M. Kaskulov and P. Grabmayr, Phys. Rev. C **67**, 042201(R) (2003); nucl-th/0308105; M.M. Kaskulov (private communication).

[Kelly 2000] J.J. Kelly, GENGEN: Event Generator for Gen Using the d(e,e'n)p Reaction, JLab E93-038 internal report (2000),
URL: *http://www.jlab.org/ semenov/reports/gengen2.5.ps*

[Kelly 2001a] J.J. Kelly, Time Calibration Procedures for E93-038 Polarimeter: Version 2.2, JLab E93-038 internal report (2001),
URL: *http://www.physics.umd.edu/enp/e93038/time_calibration.ps*

[Kelly 2003] J.J. Kelly, private communication (2003).

[Klein 1997a] F. Klein and H. Schmieden, Nucl. Phys. **A623**, 323c (1997).

[Klein 1997b] F. Klein, Proc. of the 14th Int. Conf. on Particles and Nuclei, ed. by C.E. Carlson and J.J. Domingo, World Scientific 1997, p.121.

[Kopecky 1997] S. Kopecky *et al.*, Phys. Rev. C **56**, 2229 (1997); Phys. Rev. Lett. **74**, 2427 (1995).

[Kroll 1992] P. Kroll, M. Schurmann, and W. Schweiger, Z. Phys. **A342**, 429 (1992).

[Ladygin 1999] V.P. Ladygin, Joint Institute for Nuclear Research (Dubna) preprint E13-99-123 (1999).

[Laget 1990] J.M. Laget, Phys. Lett. **B273**, 367 (1990).

[Liu 2001] K.F. Liu, Private Communication (2001).

[Lomon 2002] E. L. Lomon, Phys. Rev. C **66**, 045501 (2002); Phys. Rev. C **64**, 035204 (2001).

[Lu 1998] D.H. Lu, A.W. Thomas, and A.G. Williams, Phys. Rev. **C57**, 2628 (1998).

[Lung 1993] A. Lung *et al.*, Phys. Rev. Lett. **70**, 718 (1993).

[Ma 2002] B.-Q. Ma, D. Qing, and I. Schmidt, Phys. Rev. C **65**, 035205 (2002).

[Madey 1995] R. Madey, A. Lai, and T. Eden, Polarization Phenomena in Nuclear Physics, edited by E.J. Stephenson S.E. Vigdor, AIP Proceedings No. 339, 47-54 (1995).

[Madey 2003] R. Madey *et al.*, Phys. Rev. Lett. **91**, 122002 (2003).

[Mergell 1996] P. Mergell, U.G. Meissner, D. Drechsel , Nucl. Phys. **A596**, 367 (1996).

[Meyerhoff 1994] M. Meyerhoff *et al.*, Phys. Lett. **B327**, 201 (1994).

[Milbrath 1998] B. D. Milbrath *et al.*, Phys. Rev. Lett. **80**, 452 (1998); Phys. Rev. Lett. **82**, 2221(E) (1999).

[Miller 2002] G. A. Miller, Phys. Rev. C **66**, 032201(R) (2002); nucl-th/0206027; G. A. Miller and M. R. Frank, Phys. Rev. C **65**, 065205 (2002); M. R. Frank, B. K. Jennings, and G. A. Miller, Phys. Rev. C **54**, 920 (1996); G. A. Miller, private communication (2003).

[Miller 2007] G. A. Miller, Phys. Rev. Lett. **99**, 112001 (2007)

[Mosconi 1991] B. Mosconi, J. Pauchenwein, and P. Ricci, Proceedings of the XIII European Conference on Few-Body Problems in Physics, Marciana Marina (Elba), Italy (September 1991).

[Ohlsen 1973] G.G. Ohlsen and P.W. Keaton, Jr., Nucl. Instr. Meth. **109**, 41 (1973).

[Pace 2000] E. Pace, G. Salme, F. Cardarelli, and S. Simula, Nucl. Phys. **A666**, 33 (2000).

[Passchier 1999] I. Passchier *et al.*, Phys. Rev. Lett. **82**, 4988 (1999).

[Plaster 2006] B. Plaster *et al.* , Phys. Rev. **C73**, 025205 (2006).

[Platchkov 1990] S. Platchkov *et al.*, Nucl. Phys. **A508**, 343c (1990).

[Pospischil 2001] Th. Pospischil *et al.*, Eur. Phys. J. A **12**, 125 (2001).

[Radyushkin 1984] A.V. Radyushkin, Acta Phys. Polon. **B15**, 403 (1984).

[Rekalo 1989] M.P. Rekalo, G.I. Gakh, and A.P. Rekalo, J. Phys. **G15**, 1223 (1989).

[Riordan 10] S. Riordan et al., arXiv:1008.1738v1 (2010).

[Rock 1992] S. Rock *et al.*, Phys. Rev. D **46**, 24 (1992).

[De Sanctis 2000] M. De Sanctis, M.M. Giannini, L. Repetto, and E. Santopinto, Phys. Rev. **C62**, 025208 (2000).

[Schiavilla 2001] R. Schiavilla and I. Sick, Phys. Rev. **C64**, 041002 (2001).

[Schmieden 1996] H. Schmieden, Proc. of the 12th Int. Symposium on High-Energy Spin Physics, Amsterdam (1996), ed. by C.W. de Jager et al., World Scientific 1997, p.538.

[Semenov 2010] A.Yu. Semenov, AIP Conf. Proc. 1257, 661 (2010).

[Semenova 2003] I.A. Semenova, A.Yu. Semenov, and R. Madey, Simulation of the Efficiency of the E93-038 Neutron Polarimeter with the FLUKA code, JLab E93-038 internal report (2003).

[Theis 2006] C. Theis *et al.*, Nucl. Instrum. Meth. **A562**, 827 (2006).

[Ulmer 1991] P.E. Ulmer, MCEEP – Monte Carlo for Electro-Nuclear Coincidence Experiments, CEBAF–TN–91–101 (1991).

[Venkat 2010] S. Venkat, J. Arrington, G. A. Miller and X. Zhan, arXiv:1010.3629 [nucl-th].

[Warren 2004] G. Warren *et al.*, Phys. Rev. Lett. **92**, 042301 (2004).

[Zeitnitz 1994] C. Zeitnitz and T.A. Gabriel, Nucl. Instrum. Meth. **A349**, 106 (1994).

[Zhu 2001] H. Zhu *et al.*, Phys. Rev. Lett. **87**, 081801 (2001).

Appendix A: Suppression of Inelastic Events

1 Results from E93-038

Extraction of a reliable result for G_E^n from the quasielastic $d(\vec{e}, e'\vec{n})p$ reaction requires the suppression of inelastic events associated with pion production. To illustrate, correlation plots of the missing momentum, $p_{\rm miss}$, plotted versus the invariant mass, W, are shown for the E93-038 acceptance of the two highest Q^2 points: 1.136 and 1.474 $({\rm GeV}/c)^2$. As can clearly be seen there, quasielastic events were associated with missing momenta in the range < 150 MeV/c. Larger values of $p_{\rm miss}$ were, of course, seen to correspond to inelastic events, with the $\Delta(1232)$ resonance prominent at large missing momenta in the $Q^2 = 1.474$ $({\rm GeV}/c)^2$ spectrum.

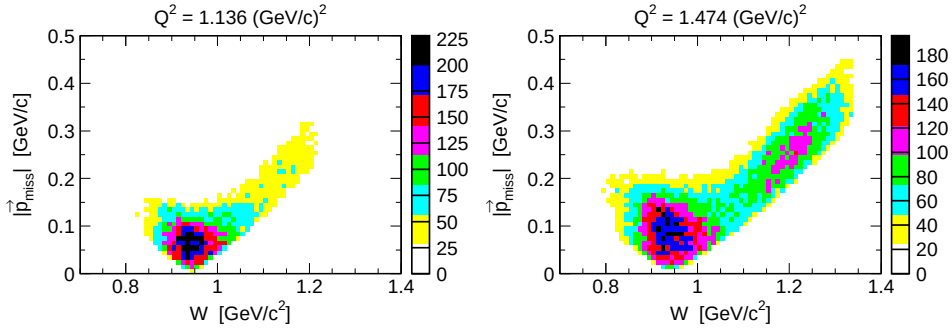

Figure 33: Correlation plot of $p_{\rm miss}$ versus W for the E93-038 acceptance at $Q^2 = 1.136$ and 1.474 $({\rm GeV}/c)^2$.

In E93-038, these inelastic events were suppressed with tight cuts on $\Delta p/p$ ($-3/+5\%$), $p_{\rm miss}$ (< 100 MeV/c), and cTOF ($\in [-1, 1]$ ns). As evidence these cuts suppressed inelastic events, invariant mass spectra obtained before and after these cuts are shown in Fig. 34 for these two Q^2 points. It is quite clear that after all cuts, the distributions converged to fairly narrow peaks centered on the neutron mass.

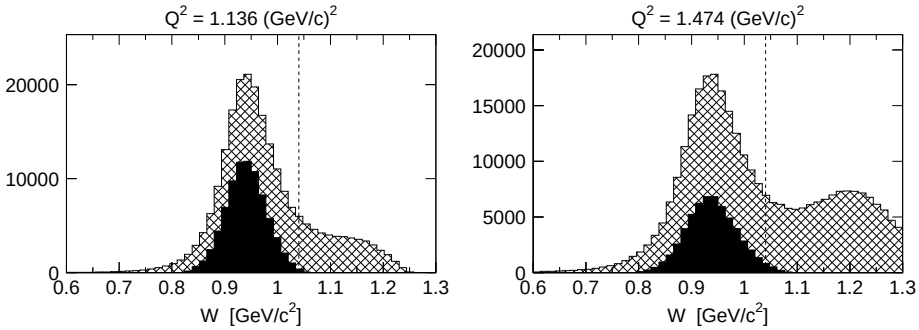

Figure 34: Distributions from E93-038 of the invariant mass W before (cross-hatched) and after (solid) all cuts except for those on $\Delta p/p$, $p_{\rm miss}$, and cTOF at $Q^2 = 1.136$ and 1.474 $({\rm GeV}/c)^2$. The vertical dashed lines denote the final E93-038 $W < 1.04$ GeV/c^2 cut.

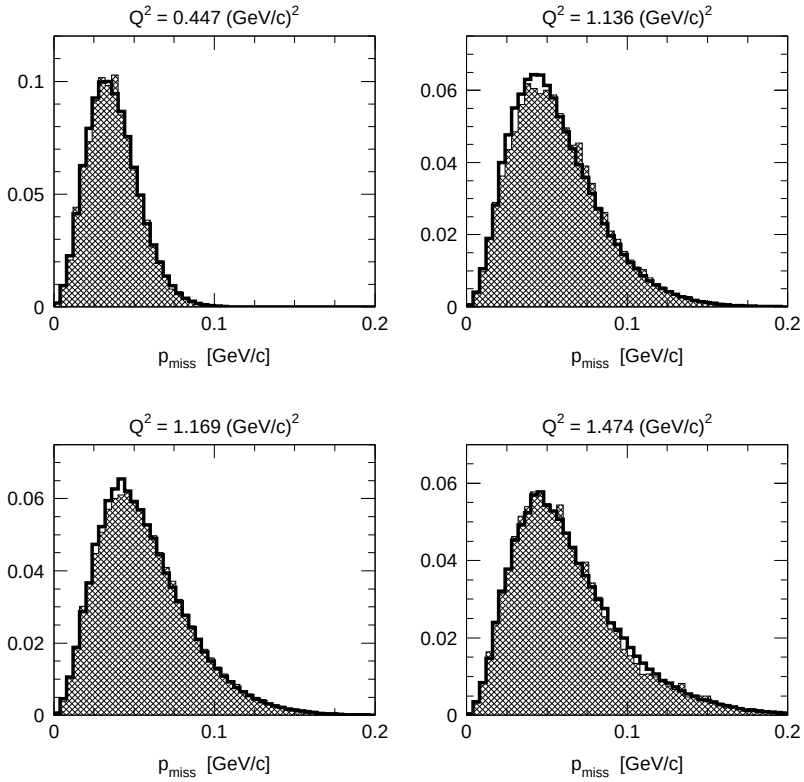

Figure 35: Comparison of GENGEN simulated (unfilled histograms with thick solid line borders) and experimental (cross-hatched filled histograms) distributions of $p_{\rm miss}$ for the four central E93-038 Q^2 points. Identical cuts were applied to both the simulated and experimental data.

2 Simulation results for kinematics similar to this proposal

To demonstrate the efficiency of the suppression of inelastic events for kinematics similar to this proposal, the GENGEN simulation code [1] was used to generate invariant mass spectra for quasielastic $d(e,e'n)p$ and inelastic $d(e,e'n\pi)$ events. This simulation code was developed to perform the kinematic acceptance-averaging and calculation of the FSI, MEC, and IC corrections for E93-038. The simulation includes an event generator for quasielastic and pion-production reactions, a model for the acceptance of a magnetic spectrometer, spin transport through the Charybdis dipole field, and a detailed model of the NPOL acceptance and interactions (including nucleon-nucleon scattering inside the polarimeter). Good agreement with experimental distributions was achieved, as shown in Fig. 35 where GENGEN simulated and experimental distributions of $p_{\rm miss}$ are compared for the four E93-038 central Q^2 points.

Note that quasielastic and inelastic events were not simulated simultaneously, because of the difficulty of developing such an event generator for a two-particle coincidence experiment.* Thus, to understand the efficiency of the suppression of inelastic events (relative to the selection of quasielastic events), it was necessary to normalize the separately simulated quasielastic and

*Simultaneous simulation of the quaisfree $d(e,e'n)p$ knockout (from a moving nucleon) and inelastic pion production (upon a moving nucleon) reactions is complicated by the fact that the knockout reaction is 5-fold differential, whereas that for pion production is 6-fold differential (in the presence of an undetected particle). Thus, simultaneous simulation of these reactions in a realistic, and efficient, manner is a non-trivial problem [2].

Data	Q^2 [(GeV/c)^2]	E_e [GeV]	$E_{e'}$ [GeV]	$\theta_{e'}$ [deg]	θ_n [deg]	T_n [GeV]
NE-11	4.00	5.507	3.377	26.8°	31.4°	2.130
E133	7.11	17.307	13.523	10.0°	30.5°	3.784

Table 6: Simulated SLAC NE-11 and E133 kinematics.

inelastic spectra to experimental results for W spectra. Simulations were performed for the kinematics of two experiments with Q^2 values similar to those in this proposal: SLAC NE-11 [3], reporting results for G_E^n from $Q^2 = 1.75$ to 4.00 (GeV/c)^2; and SLAC E133 [4], reporting results for the elastic electron-neutron cross section from $Q^2 = 2.5$ to 10.0 (GeV/c)^2. Both experiments reported measurements of W spectra for $d(e, e')$ scattering near the quasielastic peak and into the inelastic region. Simulations were performed for a subset of the kinematics from these experiments; results are shown below for the kinematics listed in Table 6.

Results from simulations of the SLAC NE-11 $Q^2 = 4.00$ (GeV/c)^2 kinematics are shown in Fig. 36. The top panel shows the simulated invariant mass spectra normalized to the experimental data, whereas the bottom panel shows the spectra after application of the nominal cuts for this proposal: $\Delta p/p = -3/+15\%$, |cTOF| < 1 ns, and $p_{\rm miss} < 100$ MeV/c. With these cuts, the contamination from inelastic events is estimated to be small, $\sim 1\%$, for a proposed invariant mass cut of $W < 1.1$ GeV/c^2. After all cuts, the quasielastic event yield, relative to the original simulated quasielastic distributions prior to cuts, was calculated to be 57%. With a less stringent cut of $p_{\rm miss} < 250$ MeV/c, the inelastic contamination increases to $\sim 6\%$ (shown in Fig. 37) for $W < 1.1$ GeV/c^2, while the quasielastic yield increases only slightly to 69%.

Results from simulations of the SLAC E133 $Q^2 = 7.11$ (GeV/c)^2 kinematics are shown in Fig. 38. Here, even though the ratio of the initial inelastic to quasielastic event population is greater (with a broader quasielastic peak), the inelastic contamination is still small, $\sim 3\%$, for $p_{\rm miss} < 100$ MeV/c and $W < 1.1$ GeV/c^2. The quasielastic event yield was calculated to be 47%. The simulations indicate that loosening the $p_{\rm miss}$ cut to 250 MeV/c would increase the inelastic contamination to $\sim 8\%$ (see Fig. 39), while only increasing the quasielastic yield slightly from 47% to 59%. To summarize, simulations of the measurement proposed here in which a magnetic spectrometer is employed for detection of the scattered electron indicate that contamination from inelastic events will be small with a tight cut on $p_{\rm miss}$. The simulations also indicate that the quasielastic event yield will also be (relatively) high, even with a tight $p_{\rm miss}$ cut.

3 Simulation results for calorimeter energy resolution

Quasielastic event yields and inelastic suppression efficiencies were also extracted from simulations of a degraded energy resolution for the detection of the scattered electron. The results of these simulations are relevant for a comparison between the measurement proposed here and the proposed measurement of G_E^n utilizing a polarized ^{3}He target and a calorimeter for the measurement of the scattered electron's energy [5].

The model for the calorimeter implemented in the `GENGEN` simulation code consisted of a "black box" acceptance, with an angular acceptance similar to that of the BigCal calorimeter (assumed to be positioned 10 m from the target) and an energy resolution (assumed to be purely Gaussian) of $\sigma_E = 5\%/\sqrt{E}$. Invariant mass spectra were generated for both the SLAC NE-11 $Q^2 = 4.00$ (GeV/c)^2 kinematics, and also the SLAC E133 $Q^2 = 7.11$ (GeV/c)^2 kinematics.

In the analysis of the data from the calorimeter simulations, the relative quasielastic/inelastic normalizations from the spectrometer simulations were retained (as the normalizations relate the relative underlying quasielastic/inelastic distributions, which are then folded with the acceptance and resolution).

Note that the SLAC NE-11 $Q^2 = 4.00$ (GeV/c)^2 kinematics are quite similar to those for the proposed polarized ^{3}He target / calorimeter measurement at $Q^2 = 5.00$ (GeV/c)^2, in which $E_e = 5.85$ GeV, $E_{e'} = 3.19$ GeV, and $\theta_{e'} = 30.0^\circ$ [5]. Results from the calorimeter simulation for the SLAC NE-11 $Q^2 = 4.00$ (GeV/c)^2 kinematics are shown in the top panel of Fig. 40. As would be expected, these spectra are significantly broader than those shown for the magnetic spectrometer simulation. Despite these broader shapes, the inelastic contamination, shown in the bottom panel of Fig. 40, is still small for a tight $p_{\rm miss} < 100$ MeV/c cut, with the contamination estimated to be $\sim 1\%$. However, the quasielastic yield for this $p_{\rm miss}$ cut is only 33%. With a less stringent $p_{\rm miss} < 250$ MeV/c cut (see Fig. 41), the inelastic contamination increases to $\sim 4\%$, while the quasielastic yield increases to 55%. These results can be understood by comparing the $p_{\rm miss}$ distributions from the magnetic spectrometer and calorimeter simulations. As shown in Fig. 42, the degraded energy resolution of the calorimeter distorts the $p_{\rm miss}$ distributions, by "stretching" the spectra to larger values of $p_{\rm miss}$ away from $p_{\rm miss} = 0$.

Finally, results from the calorimeter simulation for the SLAC E133 $Q^2 = 7.11$ (GeV/c)^2 kinematics are shown in the top panel of Fig. 43. Again, these spectra are significantly broader than those from the magnetic spectrometer simulation. The inelastic contamination with a tight $p_{\rm miss} < 100$ MeV/c cut is estimated to be (very) small, $\sim 0.1\%$; however, the quasielastic yield is calculated to be small, $\sim 20\%$. With a looser $p_{\rm miss} < 250$ MeV/c cut (see Fig. 44), the inelastic contamination increases to $\sim 2\%$, and the quasielastic yield increases to $\sim 39\%$. Distributions of $p_{\rm miss}$ from the magnetic spectrometer and calorimeter simulations for these kinematics are shown in Fig. 45.

4 Summary

In summary, the simulations suggest that the relative inelastic contamination for both types of experiments, either with a magnetic spectrometer or a calorimeter for the measurement of the scattered electron's energy, can be reduced to a small level with a tight cut on the missing momentum; however, the simulations do suggest that the degraded energy resolution of the calorimeter will result in a significantly reduced quasielastic yield, as compared to the quasielastic yields in the magnetic spectrometer simulations.

It should be noted that the response of the calorimeter implemented in these simulations was highly simplistic, in that the energy resolution was assumed to be purely Gaussian with $\sigma_E = 5\%/\sqrt{E}$. A broader resolution, or the presence of a tail, would almost certainly lead to a greater distortion of the missing momentum distribution, resulting in an even smaller quasielastic yield.

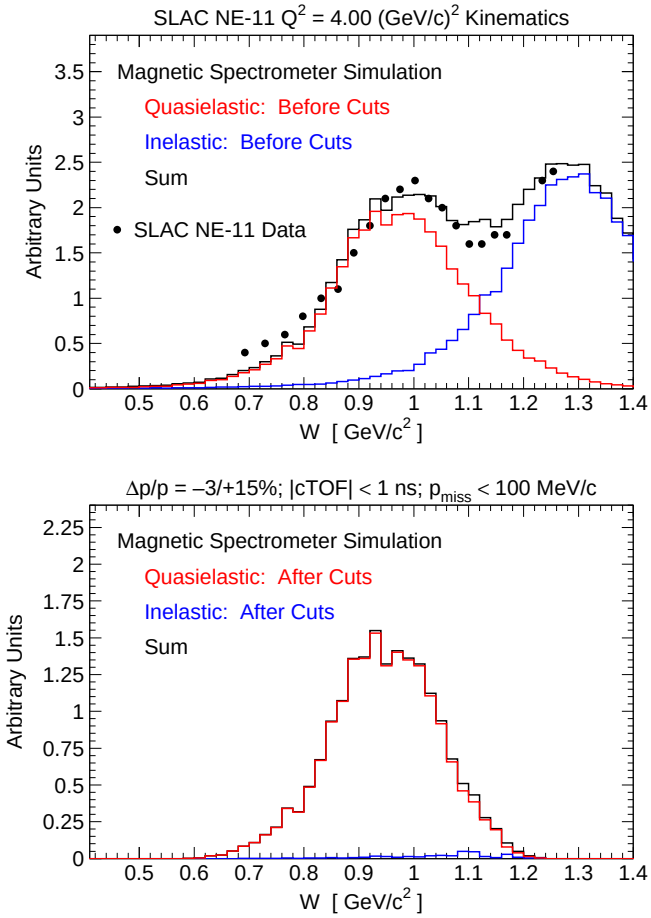

Figure 36: (Top panel) Results from simulations of quasielastic and inelastic invariant mass spectra for the $Q^2 = 4.00$ (GeV/c)^2 kinematics of SLAC NE-11. (Bottom panel) Invariant mass spectra after application of cuts. The inelastic contamination is estimated to be $\sim 1\%$ for $W < 1.1$ GeV/c^2.

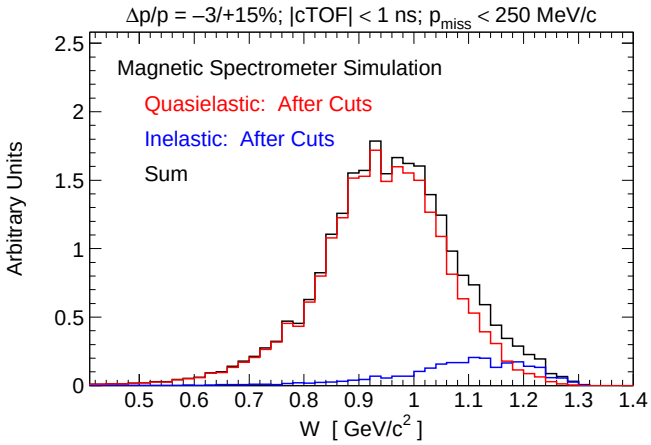

Figure 37: Invariant mass spectra after application of a less stringent $p_{\rm miss} < 250$ MeV/c cut. The inelastic contamination is estimated to be $\sim 6\%$ for $W < 1.1$ GeV/c^2.

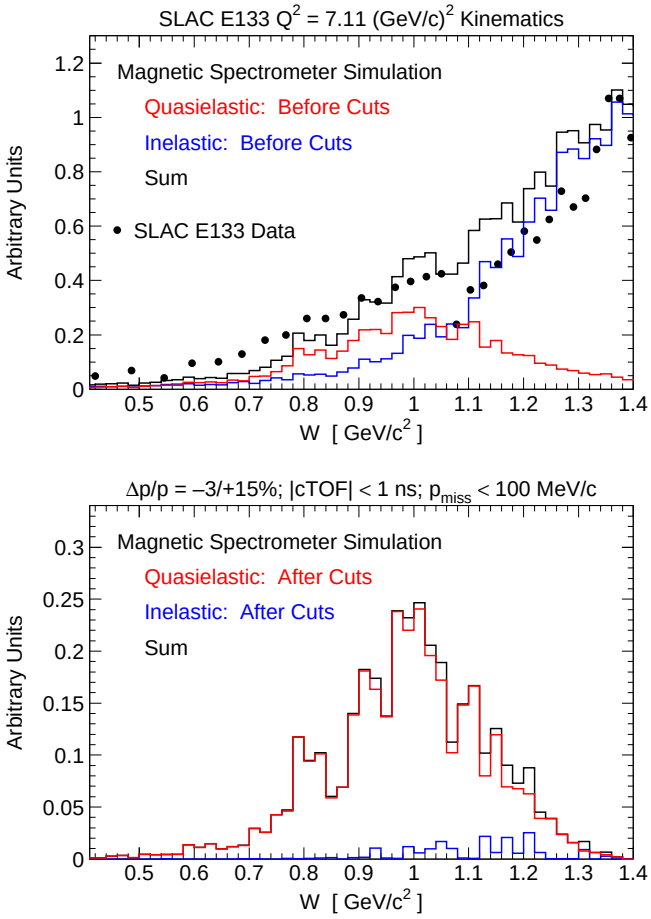

Figure 38: (Top panel) Results from simulations of quasielastic and inelastic invariant mass spectra for the $Q^2 = 7.11$ (GeV/c)^2 kinematics of SLAC E133. (Bottom panel) Invariant mass spectra after application of cuts. The inelastic contamination is estimated to be $\sim$ 3% for $W < 1.1$ GeV/c^2.

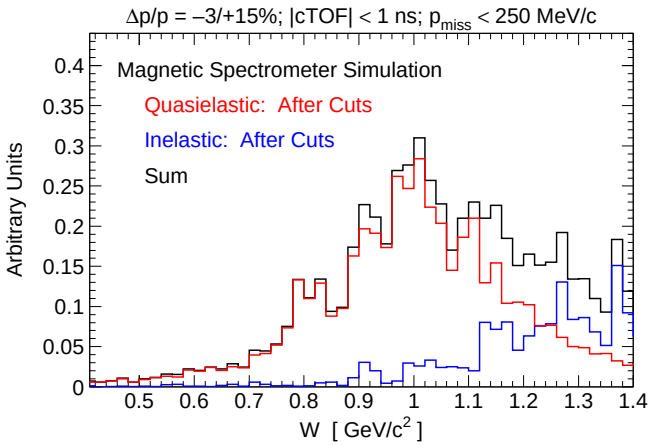

Figure 39: Invariant mass spectra at $Q^2 = 4.00$ (GeV/c)^2 after application of a less stringent $p_{\rm miss} < 250$ MeV/c cut. The inelastic contamination is estimated to be $\sim$ 8% for $W < 1.1$ GeV/c^2.

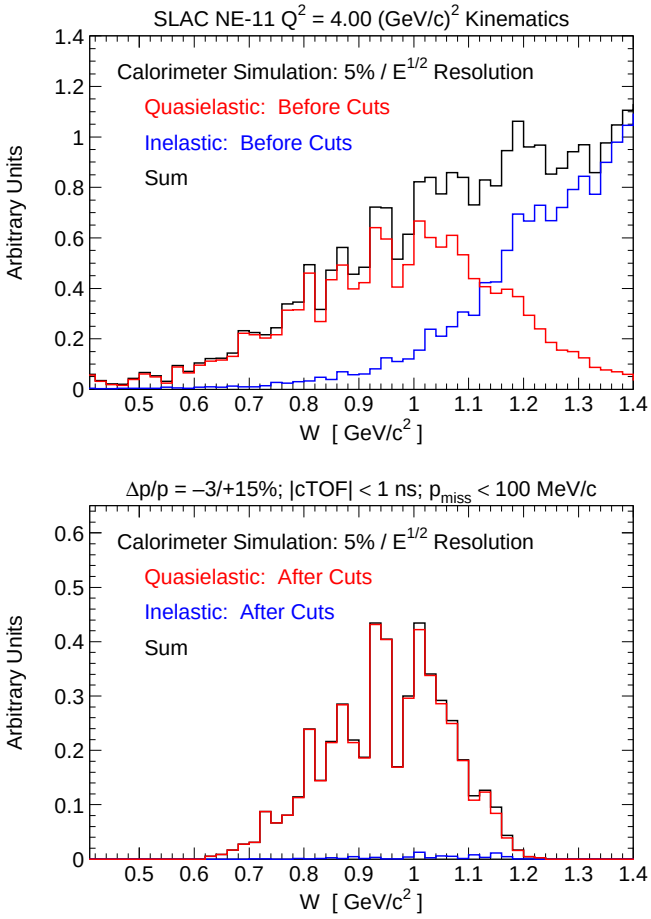

Figure 40: (Top panel) Results from simulations of quasielastic and inelastic invariant mass spectra for the $Q^2 = 4.00$ (GeV/c)^2 kinematics of SLAC NE-11, assuming a calorimeter measurement of the scattered electron energy with an energy resolution of $\sigma_E = 5\%/\sqrt{E}$. Top panel: spectra before application of cuts. (Bottom panel) Invariant mass spectra after application of cuts. The inelastic contamination is estimated to be $\sim 1\%$ for $W < 1.1$ GeV/c^2.

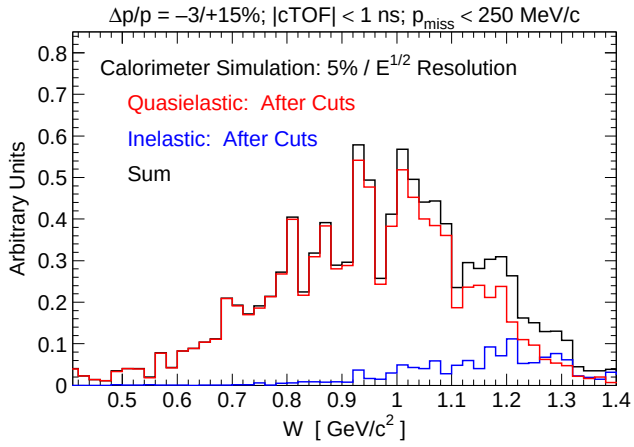

Figure 41: Invariant mass spectra at $Q^2 = 4.00$ (GeV/c)^2 after application of a less stringent $p_{\rm miss} < 250$ MeV/c cut. The inelastic contamination is estimated to be $\sim 4\%$ for $W < 1.1$ GeV/c^2.

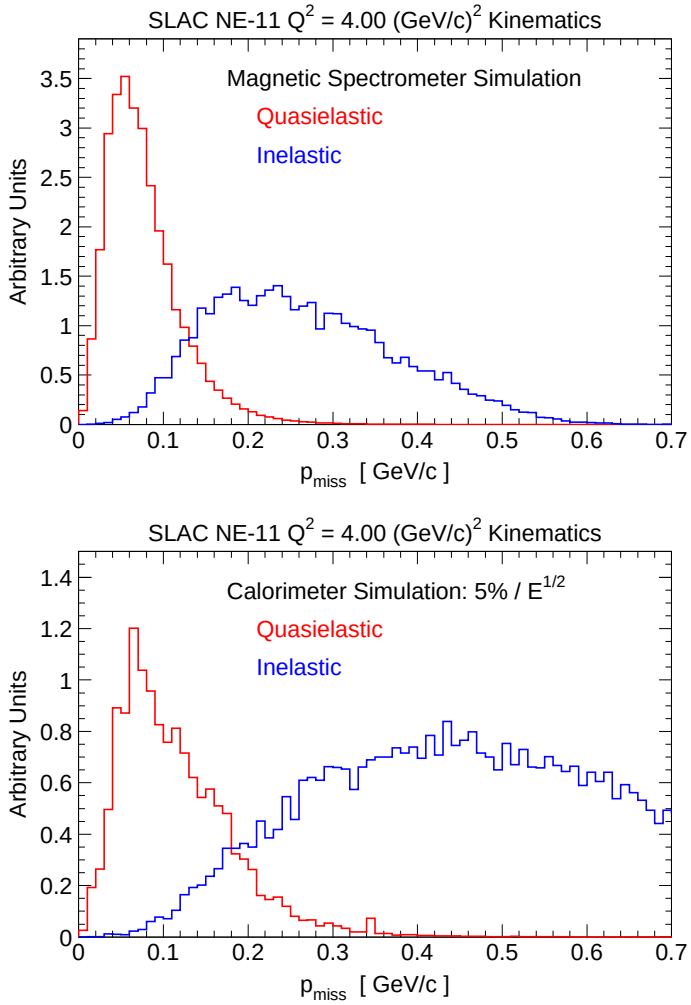

Figure 42: Missing momentum distributions for quasielastic and inelastic events from magnetic spectrometer (top panel) and calorimeter (bottom panel) simulations for the SLAC NE-11 $Q^2 = 4.00$ (GeV/c)^2 kinematics.

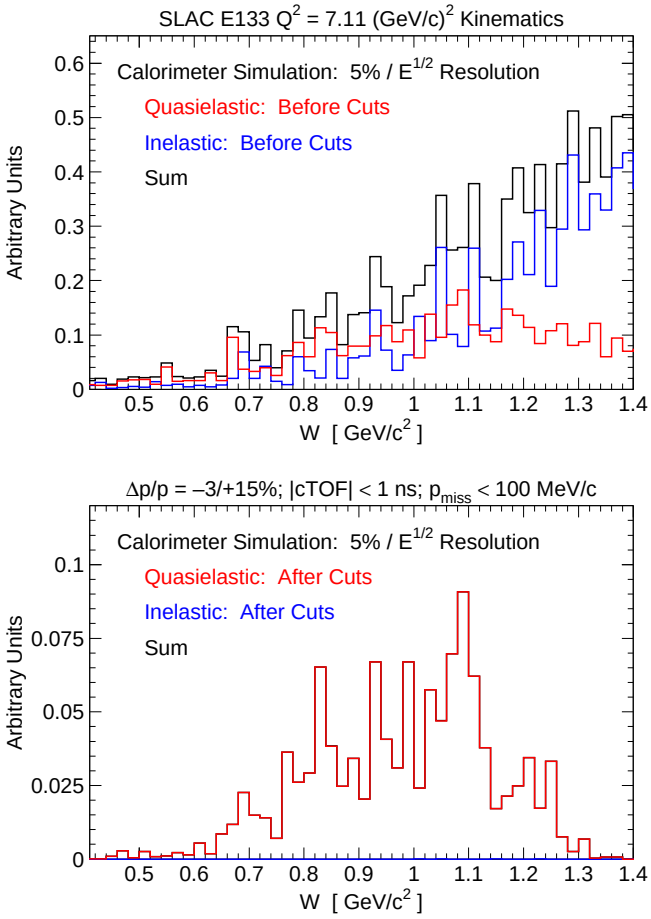

Figure 43: (Top panel) Results from simulations of quasielastic and inelastic invariant mass spectra for the $Q^2 = 7.11$ (GeV/c)^2 kinematics of SLAC E133, assuming a calorimeter measurement of the scattered electron energy with an energy resolution of $\sigma_E = 5\%/\sqrt{E}$. Top panel: spectra before application of cuts. (Bottom panel) Invariant mass spectra after application of cuts. The inelastic contamination is estimated to be $\sim 0.1\%$ for $W < 1.1$ GeV/c^2.

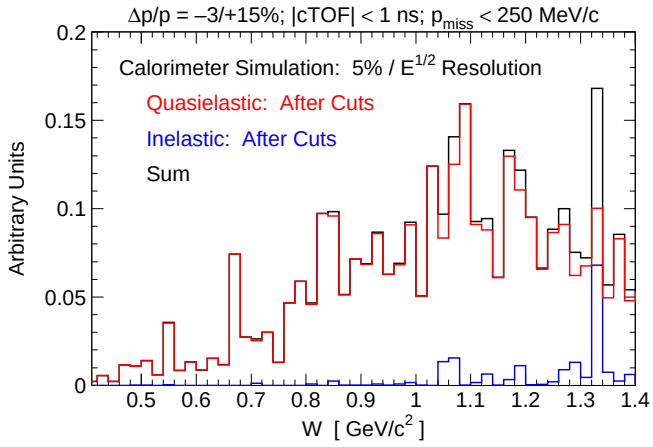

Figure 44: Invariant mass spectra at $Q^2 = 7.11$ (GeV/c)^2 after application of a less stringent $p_{\rm miss} < 250$ MeV/c cut. The inelastic contamination is estimated to be $\sim 2\%$ for $W < 1.1$ GeV/c^2.

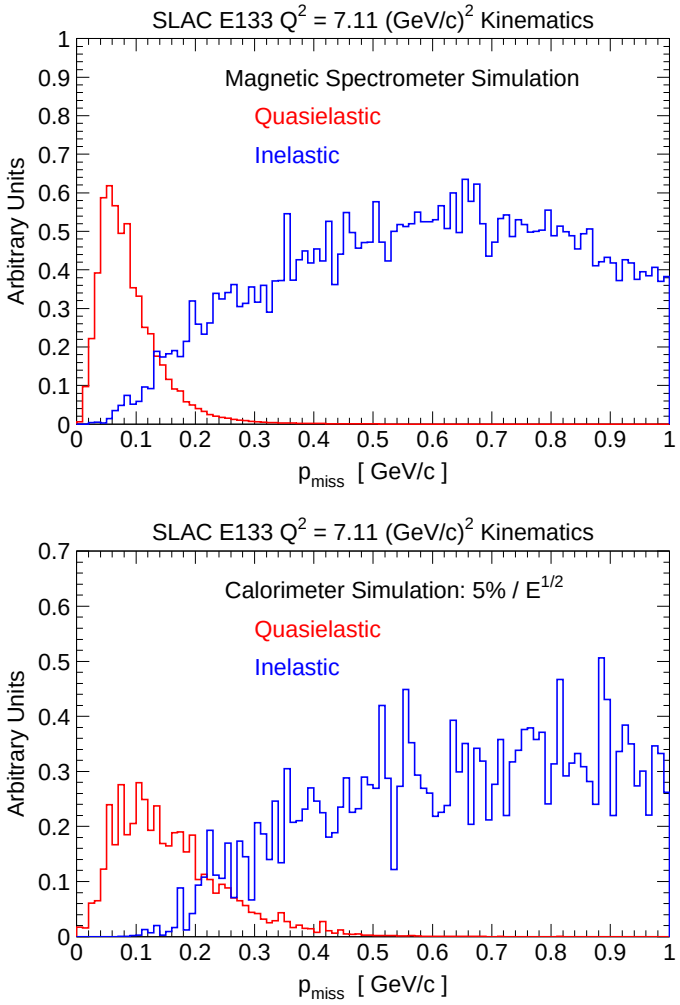

Figure 45: Missing momentum distributions for quasielastic and inelastic events from magnetic spectrometer (top panel) and calorimeter (bottom panel) simulations for the SLAC E133 $Q^2 = 7.11$ (GeV/c)^2 kinematics.

References

[1] B. Plaster *et al.*, Phys. Rev. C **73**, 025205 (2006).

[2] J. J. Kelly, private communication (2003).

[3] A. Lung *et al.*, Phys. Rev. Lett. **70**, 718 (1993).

[4] S. Rock *et al.*, Phys. Rev. D **46**, 24 (1992).

[5] G. Cates, Talk at the Second Super BigBite Workshop, September 5, 2008, `hallaweb.jlab.org/12GeV/SuperBigBite/meetings/02/agenda.html`